

## Spatial and Chemical Complexity in the W75N Star-Forming Region

MORGAN M. GIESE <sup>1</sup>, WILL E. THOMPSON <sup>2</sup>, DARIUSZ C. LIS <sup>3</sup>, AND  
SUSANNA L. WIDICUS WEAVER <sup>1,2</sup>

<sup>1</sup>*Department of Astronomy, University of Wisconsin-Madison  
475 N Charter St, Madison, Wisconsin 53706, USA*

<sup>2</sup>*Department of Chemistry, University of Wisconsin-Madison  
1101 University Ave, Madison, Wisconsin 53706, USA*

<sup>3</sup>*Jet Propulsion Laboratory, California Institute of Technology  
4800 Oak Grove Drive, Pasadena, CA, 91109, USA*

### ABSTRACT

We present the analysis of NOEMA interferometric observations of the high-mass star-forming region W75N(B) with a focus on molecular composition and distribution of prebiotic molecules in the source’s multiple cores. Over twenty molecules are identified across the region, with many being fit for column density, rotational temperature, spectral line full width half maximum, and  $v_{lsr}$ . This work includes the first known detection and initial analysis of complex organic molecules in the MM2 and MM3 regions. Furthermore, parameter maps were created from the six molecules that were well fit across multiple regions. The molecular emission was imaged and correlated across different molecules and the continuum to reveal structural features. From the spatial and spectral analysis of the MM1 region, these results concur with those from other studies showing that there is a difference in chemical composition between the MM1a and MM1b regions, with sulfur-bearing molecules tracing MM1a and organic molecules tracing MM1b. The molecular emission imaged toward the MM3 region reveals two peaks, possibly indicating the presence of multiple young stellar objects. These results provide detailed quantitative information about the physical parameters and distributions of molecules in this source. Additionally, these results are part of a follow-up of a single-dish survey of multiple star-forming regions and are discussed in this context.

*Keywords:* Astrochemistry (75) — Star-forming regions (1565) — Interferometry (808)

### 1. INTRODUCTION

Broadband line surveys provide a means to detect and quantify the molecular compositions of interstellar sources. For star-forming regions in particular, such surveys enable identification and analysis of complex organic molecules (COMs), defined as having more than six atoms, that could serve as precursors for life. COMs can be found in abundance in star-forming regions and protoplanetary disks, and these molecules play a role in the formation of planetary systems (Blake & van Dishoeck 1998; van Dishoeck 2006). Many of these prebiotic molecules are generally formed from

the photo and thermal processing of icy dust grains, from which they ultimately sublimate into the gas phase (Munoz Caro et al. 2002; Öberg et al. 2011; Altwegg et al. 2019). Once in the gas phase, interferometric studies become essential for probing the chemical composition and distribution of molecules in different star-forming regions. Interferometers such as the Northern Extended Millimeter Array (NOEMA) and the Atacama Large Millimeter/Submillimeter Array (ALMA) allow for targeted observations with high spatial and spectral resolution to characterize these chemically-rich environments (Jørgensen et al. 2004; Tobin et al. 2011; Tychoniec et al. 2021).

W75N(B) is a high-mass star-forming region in the Cygnus X molecular cloud located at a distance of  $\sim 2$  kpc with a  $v_{lsr}$  of  $10 \text{ km s}^{-1}$  (Haschick et al. 1981; Minh et al. 2010; van der Walt et al. 2021). W75N(B) (hereafter simply W75N) is associated with three millimeter continuum cores MM1, MM2, and MM3; the brightest core MM1 is further categorized into the sub-regions MM1a and MM1b (Hunter et al. 1994; Shepherd et al. 2003; Minh et al. 2010; van der Walt et al. 2021). In addition to these sub-regions, three ultra-compact HII regions VLA1, VLA2, and VLA3 are detected, with VLA3 being cospatial with MM1a (Hunter et al. 1994; Torrelles et al. 2003; Shepherd et al. 2003). The HII regions are associated with multiple masers: VLA1 and VLA2 with OH, H<sub>2</sub>O, and CH<sub>3</sub>OH masers and VLA3 with a H<sub>2</sub>O maser (Torrelles et al. 2003; Minier et al. 2001; Shepherd et al. 2003; Hutawarakorn et al. 2002; Fish et al. 2005; Surcis et al. 2009).

Recent chemical studies of W75N include observations with the Submillimeter Array (SMA) in the 316 to 329 GHz window (van der Walt et al. 2021); with the Caltech Submillimeter Observatory (CSO) in the 220 to 267 GHz window (Widicus Weaver et al. 2017); and with the SMA in the 215 and 345 GHz windows (Minh et al. 2010). These observations all focused on the chemical composition of the MM1 region. It was determined that MM1a and MM1b display distinct spatial morphologies of organic and sulfur-bearing molecules. However, none of these studies provide detailed analysis on the molecular composition of the MM2 or MM3 regions. To add further information to these previous studies, presented here is an analysis of the molecular composition of the MM1a, MM1b, MM2, and MM3 regions along with a characterization of the spatial distribution of the discovered molecules. Below we present the details of our NOEMA observations of W75N, the spectral and spatial results of these observations for each molecule detected, and a discussion of the implications of these results in the context of COM formation in star-forming cores. As this work is part of a follow-up NOEMA survey of multiple star-forming cores originally analyzed in Widicus Weaver et al. (2017) using the CSO, molecules identified herein are also directly compared with those identified in sources previously imaged with NOEMA.

## 2. OBSERVATIONS

W75N was observed using the IRAM/NOEMA interferometer<sup>1</sup> with the A configuration for  $\sim 8$  hours on February 13 and 28 2022. The pointing center of the observations was  $\alpha(\text{J2000}) = 20^{\text{h}}38^{\text{m}}36.25^{\text{s}}$ ,  $\delta(\text{J2000}) = 42^{\circ}37'33''.0$ . The observations were centered at a local oscillator frequency of 145.250 GHz with frequency coverage from 127.823 - 135.311 GHz and 143.116 - 150.666 GHz for the lower and upper sidebands, respectively.

The baselines of the array ranged from 32.0 m to 920.0 m in the 12A configuration. The data were obtained using the PolyFiX correlator, which gave a channel spacing of 2.0 MHz across both sidebands. In addition, 28 high-resolution spectral windows were selected within the two sidebands with

<sup>1</sup> IRAM is supported by INSU/CNRS (France), MPG (Germany), and IGN (Spain).

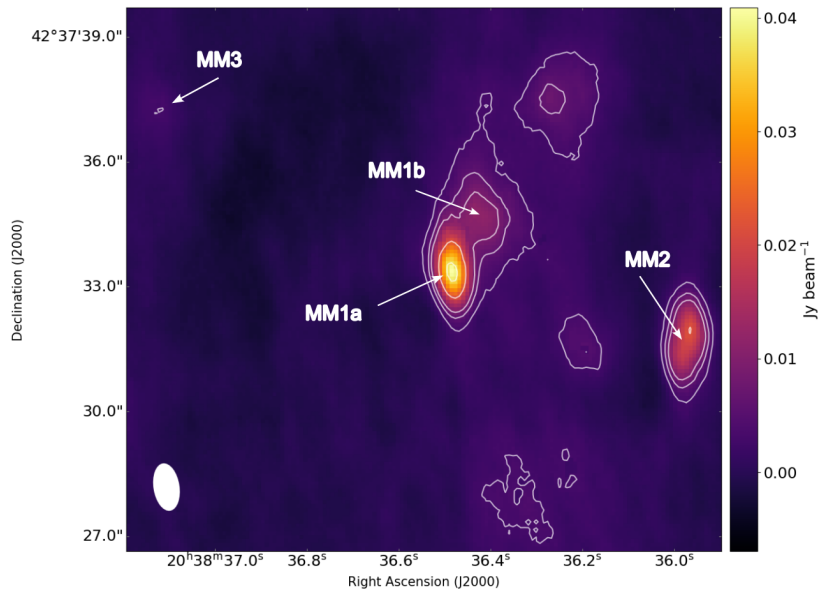


**Figure 1.** 130 GHz continuum emission of the MM1, MM2, and MM3 regions. White contour levels are at 1, 2, 3, 7, and 12 times  $\sigma$  ( $\sigma = 3.079 \text{ mJy beam}^{-1}$ ). The synthesized beam size is shown in the lower left corner.

channel spacings of  $62.5 \text{ kHz}$  ( $0.13 \text{ km s}^{-1}$ ). Bandpass calibration was performed using observations of 2013+370, and flux calibration was performed using observations of MWC349 and 2010+723. The maximum recoverable scale was  $8''.0$ , which was calculated using Equation 3.28 in Cortes et al. (2024). Phase and amplitude calibration was performed using 2013+370 and J2050+363. The system temperatures varied between 60 K and 180 K during the observations. A summary of the observational setup is shown in Appendix A.

Each dataset was reduced and cleaned following a similar procedure to that described in Thompson et al. (2023) using the GILDAS packages CLIC and MAPPING<sup>2</sup>. This resulted in a synthesized beam of  $\sim 1.00'' \times 0.53''$  (PA =  $-171.79^\circ$ ) in the lower sideband and  $\sim 0.82'' \times 0.42''$  (PA =  $8.8^\circ$ ) in the upper sideband. To clean each of the 28 high-resolution datacubes, a robust weighting system was used until the maximum amplitude of the absolute value of the residual equaled twice the noise. Each datacube was then continuum-subtracted using the STATCONT software package (Sánchez-Monge et al. 2018). STATCONT determines the continuum level at each individual pixel utilizing a user-inputted RMS value for each datacube. Appendix A reports the RMS values of each cube. Figure 1 shows the imaged continuum at 130 GHz. The MM1a, MM1b, MM2, and MM3 cores are labeled in accordance with previous works (Minh et al. 2010; van der Walt et al. 2021). Compared to these studies, the continuum emission reported here is at a much lower signal-to-noise ratio. This is especially evident in the MM3 region, where only a  $1\text{-}\sigma$  contour is seen. The flux ratio between the MM3 and MM1 regions is roughly  $1/8$ . This is comparable to flux ratios seen in other works (Minh et al. 2010; Zeng et al. 2023). Additionally, an extracted spectrum from the MM3 position listed in

<sup>2</sup> <http://www.iram.fr/IRAMFR/GILDAS>

Zeng et al. (2023) yielded no detectable lines above  $3\sigma$ . Also unlike these previous studies, molecular emission is detected from all four regions and is analyzed herein.

### 3. LINE IDENTIFICATION AND ANALYSIS

The Global Optimization and Broadband Analysis Software (GOBASIC) was used to analyze each molecule in the broadband spectra. GOBASIC performs a broadband spectral analysis for multiple molecules simultaneously under the assumptions of Gaussian line shapes and local thermodynamic equilibrium (LTE) for a given molecule. For each molecule, GOBASIC derives column density in  $\text{cm}^{-2}$ , rotational temperature in K, spectral line full width half maximum ( $\Delta v$ ) in  $\text{km s}^{-1}$ , and  $v_{lsr}$  in  $\text{km s}^{-1}$ . The intricacies of GOBASIC operation are provided in Rad et al. (2016), but a brief description is provided here.

For the analysis presented herein, GOBASIC is used in a similar manner to that in previous works (Widicus Weaver et al. 2017; Zou & Widicus Weaver 2017; Wright et al. 2022; Thompson et al. 2023; Giese et al. 2024). GOBASIC utilizes molecular catalog files from both the Cologne Database for Molecular Spectroscopy (CDMS) (Müller et al. 2001, 2005) and the Jet Propulsion Laboratory (JPL) Spectral Line Catalog (Pickett et al. 1998) to perform a full broadband analysis of multiple molecules by comparing the provided catalog information to the observational spectra. Specifics on which database catalog was used for each molecule can be found in Widicus Weaver et al. (2017). From a user-inputted initial guess for each physical parameter and the partition function information from the catalog, GOBASIC creates a spectral simulation to compare to the observational data. The partition function used in the program follows the general form

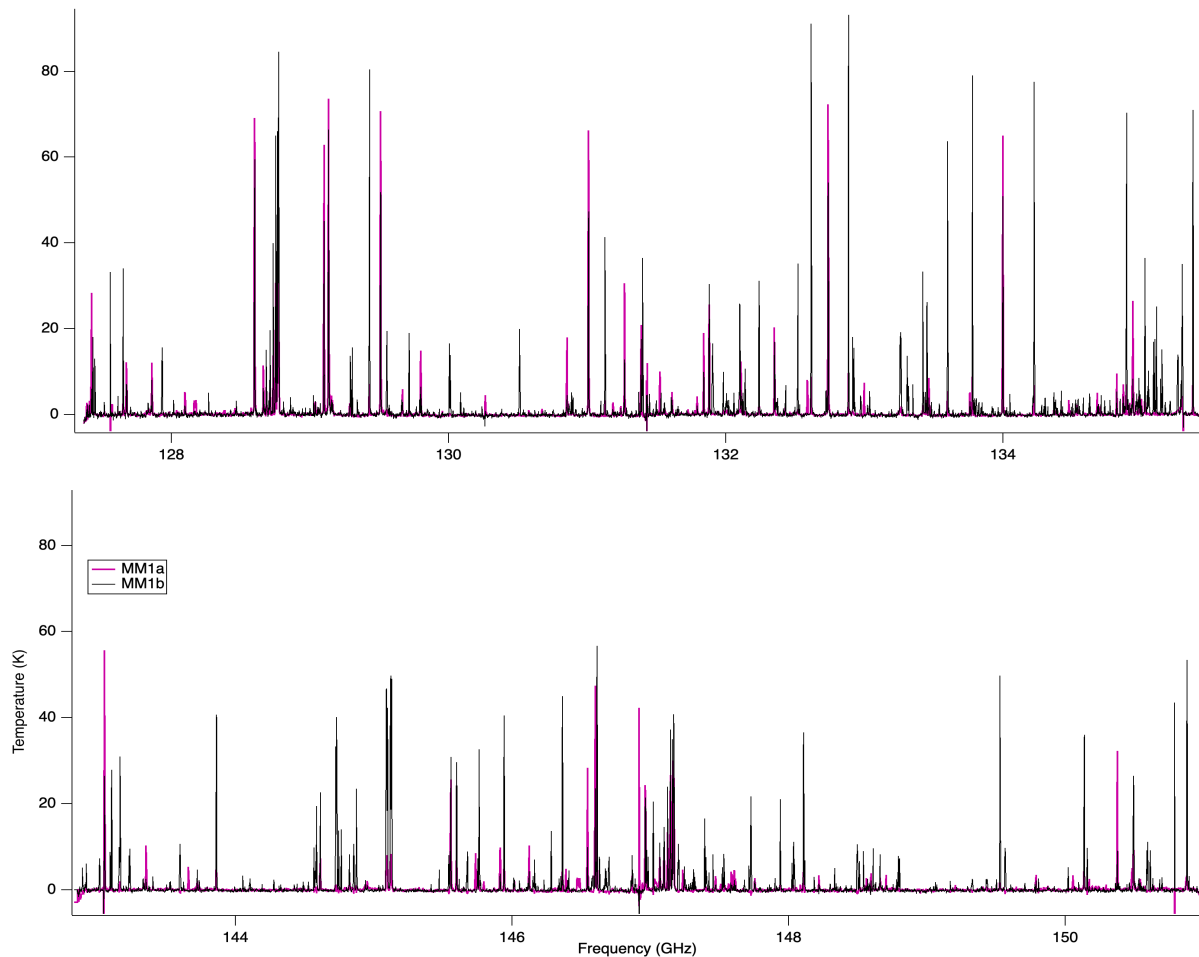
$$Q(T) = \alpha T^\beta [\gamma + \exp(\epsilon/T)]. \quad (1)$$

For most molecules identified in W75N, the coefficients for the partition function interpolation and the process by which they were calculated were previously reported in Widicus Weaver et al. (2017). Discussion on the exception to this can be found below. The values for column density, temperature, line width, and velocity were also constrained to physically-meaningful values. Furthermore, the emission is assumed to be resolved and fill the small synthesized beam. Therefore, no correction for source size was made. At the beginning of the analysis process, target molecules were chosen based on previously-published line surveys of W75N (Minh et al. 2010; Widicus Weaver et al. 2017; van der Walt et al. 2021). Any spectral lines not accounted for by molecules from these surveys were then cross-referenced with other molecular catalogs, resulting in new molecules being added to the analysis. To analyze the full region using this method, a spectrum was extracted from the pixel with peak continuum flux in each core, described in Table 1. The spectra for MM1a and MM1b can be seen in Figure 2. Spectra for MM2 and MM3 can be seen in Figure 3. Hundreds of molecular transitions were present across all four regions. As all of these transitions from all molecules were fit simultaneously using GOBASIC, a detailed analysis of each individual transition, commonly seen in other studies of star-forming regions, was not performed. All possible transitions listed in the available catalog for each molecule were included in this analysis, probing an upper energy range of 7 K to 7200 K. While not all of these transitions were visible in the low-resolution datacubes, the most intense transitions were seen in both the low-resolution and the 28 high-resolution datacubes. For these high-intensity transitions, the upper energies are provided in Table 6.

More than twenty molecules were detected in MM1a with at least three lines above  $3\sigma$ :  $\text{CH}_3\text{CN}$  (ethyl cyanide),  $\text{CH}_3\text{OH}$  (methanol),  $\text{CS}$  (carbon monosulfide),  $\text{C}^{33}\text{S}$ ,  $\text{C}^{34}\text{S}$ ,  $\text{DCN}$  (deuterium cyanide),

**Table 1.** Pixel locations with peak continuum flux used for spectral extraction.

Continuum Core	Right Ascension (J2000)	Declination (J2000)
MM1a	$20^h38^m36.5^s$	$42^\circ37'33''.3$
MM1b	$20^h38^m36.4^s$	$42^\circ37'34''.6$
MM2	$20^h38^m36.0^s$	$42^\circ37'31''.9$
MM3	$20^h38^m37.1^s$	$42^\circ37'37''.2$

**Figure 2.** Spectra for MM1a and MM1b for the lower sideband (top) and the upper sideband (bottom).

$\text{H}_2\text{CO}$  (formaldehyde),  $\text{H}_2\text{CS}$  (thioformaldehyde),  $\text{HC}_3\text{N } v_7$  (cyanoacetylene),  $\text{H}^{13}\text{CCCN}$ ,  $\text{HC}^{13}\text{CCN}$ ,  $\text{HCC}^{13}\text{CN}$ , t- $\text{HCOOH}$  (formic acid),  $\text{HDO}$  (deuterated water),  $\text{HNCO}$  (isocyanic acid),  $\text{NH}_2\text{CHO}$  (formamide),  $\text{NO}$  (nitric oxide),  $\text{OCS}$  (carbonyl sulfide),  $\text{SiO}$  (silicon monoxide),  $\text{SO}$  (sulfur monoxide),  $^{33}\text{SO}$ ,  $\text{S}^{18}\text{O}$ ,  $\text{SO}_2$  (sulfur dioxide),  $^{33}\text{SO}_2$ , and  $^{34}\text{SO}_2$ .

As DCN was not originally reported by [Widicus Weaver et al. \(2017\)](#), it was necessary to create a new interpolation of the partition function for its coefficients. The process of doing so is described in [Widicus Weaver et al. \(2017\)](#). The coefficients for interpolation, along with the line catalog database

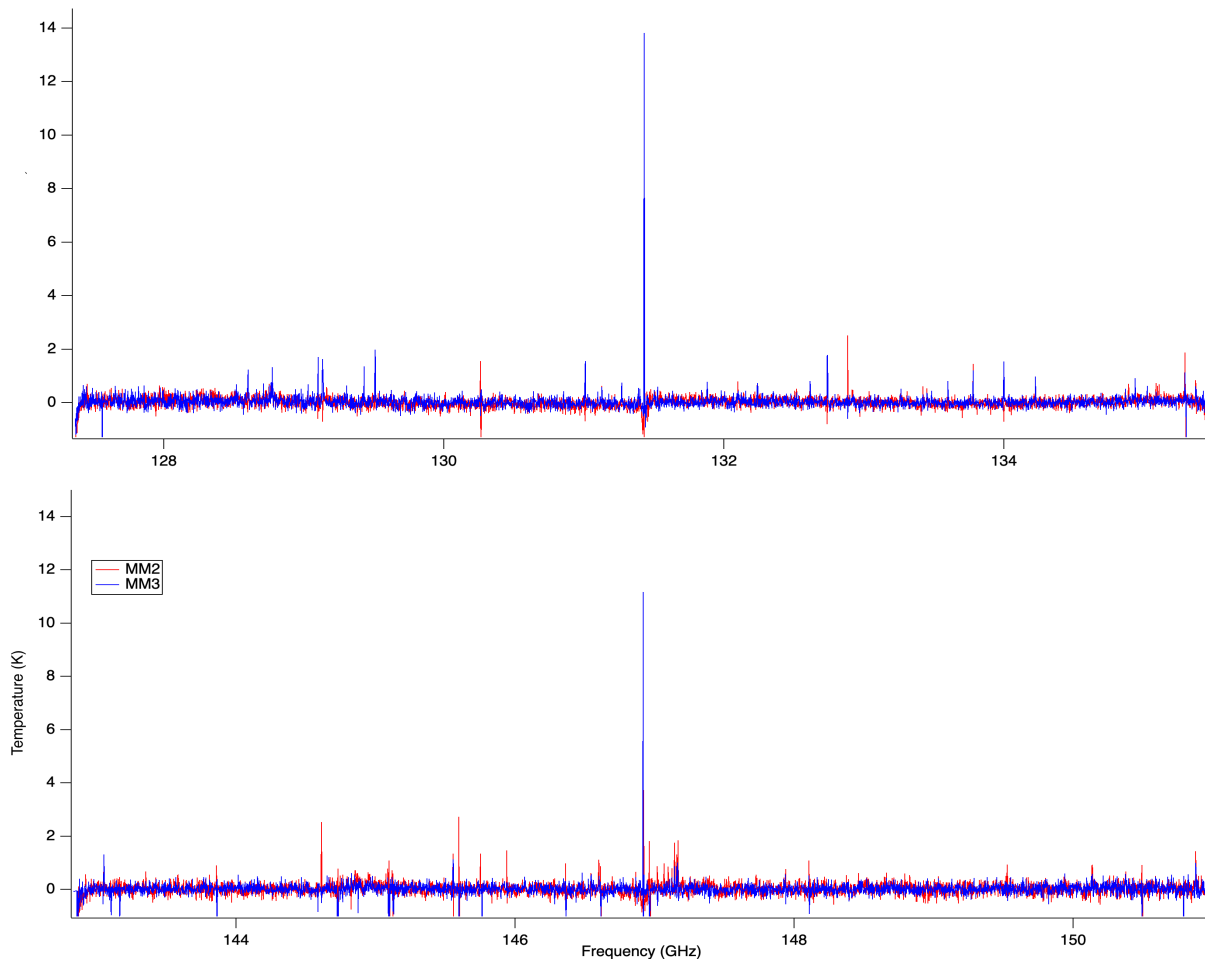


**Figure 3.** Spectra for MM2 and MM3 for the lower sideband (top) and the upper sideband (bottom).

and version, are summarized in Table 2. Similar to other molecules reported in Widicus Weaver et al. (2017), the relative deviation (defined in Equation 2) between the new interpolated partition function values and those reported in the catalog is also provided in the table.

$$\delta = Q_{interpolated}/Q_{catalog} - 1 \quad (2)$$

Physical parameters were obtained for  $\text{CH}_3\text{CN}$ ,  $\text{CH}_3\text{OH}$ ,  $\text{HC}_3\text{N } v_7$ ,  $\text{HNCO}$ ,  $\text{NH}_2\text{CHO}$ ,  $\text{OCS}$ ,  $\text{SO}$ ,  $\text{SO}_2$ , and  $^{34}\text{SO}_2$ . These molecules all have numerous lines in the spectrum, enabling a full analysis. The calculated physical parameters for these molecules are shown in Table 3. For other molecules detected in this region, it was difficult to derive accurate parameters via fitting due to each molecule having less than five observable lines over  $3\text{-}\sigma$  that were not affected by blending.

These values for molecules in MM1a are similar to those determined by van der Walt et al. (2021). Generally, the column densities are all of the same order of magnitude except for  $\text{CH}_3\text{OH}$ , which is lower in the results shown here. However, when comparing the column density of  $\text{CH}_3\text{OH}$  to that reported in Minh et al. (2010), our results match. **Some methanol lines are under-predicted by the best fit, indicating that features from other molecules were blended with these lines or additional temperature components were present for methanol.** Neither of these

**Table 2.** Partition function coefficient interpolation for DCN. Deviation between the interpolated partition function values and the catalog tabulated partition function values is listed as a range of  $[\delta_{min}, \delta_{max}]$  in units of percent.

$\alpha$	$\beta$	$\gamma$	$\epsilon$	$\delta(\%)$	Database	Version
1.727	1	0	0.5836	[0.00030 0.048]	JPL	2006 Apr

**Table 3.** Calculated physical parameters for MM1a from GOBASIC fits. The four parameters are column density in  $\text{cm}^{-2}$  ( $N_T$ ), temperature in K, spectral line full width half maximum in  $\text{km s}^{-1}$  (FWHM), and  $v_{lsr}$  in  $\text{km s}^{-1}$  ( $v_{lsr}$ ).

MM1a Derived Parameters				
Molecule	$N_T$ ( $\text{cm}^{-2}$ )	Temperature (K)	FWHM ( $\text{km s}^{-1}$ )	$v_{lsr}$ ( $\text{km s}^{-1}$ )
CH <sub>3</sub> CN	1.48(0.11)e+16	223.8(14.5)	9.44(0.19)	9.97(0.09)
CH <sub>3</sub> OH	8.38(0.82)e+16	158.0(10.4)	9.32(0.52)	10.84(0.27)
HC <sub>3</sub> N $v_7$	2.26(0.83)e+15	27.9(8.8)	10.23(0.67)	9.69(0.30)
HNCO	3.47(0.26)e+16	196.3(12.7)	8.61(0.27)	10.89(0.14)
NH <sub>2</sub> CHO	1.32(0.57)e+15	91.5(39.3)	8.88(1.03)	9.37(0.53)
OCS	2.42(0.97)e+16	13.9(2.2)	8.82(1.17)	10.65(0.56)
SO	3.92(1.30)e+17	67.7(1.0)	6.00(0.30)	9.70(0.05)
SO <sub>2</sub>	3.07(0.05)e+17	64.2(0.4)	6.70(0.04)	10.07(0.02)
<sup>34</sup> SO <sub>2</sub>	2.77(0.45)e+16	144.2(22.4)	8.60(0.46)	9.80(0.21)

cases can be fully quantified without additional information and therefore were not included in the analysis presented here. Apart from HC<sub>3</sub>N and the sulfur-bearing molecules, the temperatures reported here are higher than those in [van der Walt et al. \(2021\)](#). The FWHM values for most molecules are also generally higher than those previously reported, although the FWHM of SO<sub>2</sub> is comparable. Velocity values are also comparable. The results presented here are from an analyzed spectrum located closer to the center of the MM1a core than that of [van der Walt et al. \(2021\)](#), and this could be the cause of any discrepancies.

More than twenty molecules were also detected in MM1b with at least three lines above  $3\sigma$ : CH<sub>3</sub>CH<sub>2</sub>CN (ethyl cyanide), CH<sub>3</sub>CN, CH<sub>3</sub>OCH<sub>3</sub> (dimethyl ether), CH<sub>3</sub>OH, CS, C<sup>33</sup>S, C<sup>34</sup>S, DCN, H<sub>2</sub>CO, H<sub>2</sub>CS, HC<sub>3</sub>N  $v_7$ , H<sup>13</sup>CCCN, HC<sup>13</sup>CCN, HCC<sup>13</sup>CN, HCOOCH<sub>3</sub> (methyl formate), HDO, HNCO, NH<sub>2</sub>CHO, NO, OCS, SiO, SO, S<sup>18</sup>O, SO<sub>2</sub>, and <sup>34</sup>SO<sub>2</sub>. Physical parameters were obtained for CH<sub>3</sub>CN, CH<sub>3</sub>OCH<sub>3</sub>, CH<sub>3</sub>OH, HCOOCH<sub>3</sub>, HNCO, and SO<sub>2</sub>. These molecules each have numerous lines in the spectrum, enabling a full analysis. The calculated physical parameters for these molecules are shown in Table 4. As in the MM1a region, it was difficult to derive accurate parameters via fitting for other molecules detected in this region due to each molecule having less than five observable lines over  $3\sigma$  that were not affected by blending.

Similar to the MM1a region, all column density values of molecules in MM1b are consistent with those reported in [van der Walt et al. \(2021\)](#). In terms of temperature, CH<sub>3</sub>OCH<sub>3</sub> and HNCO are also similar to the previously reported values. CH<sub>3</sub>OH is considerably warmer with a temperature of 205 K compared to the previously reported value of 140 K, while CH<sub>3</sub>CN and SO<sub>2</sub> are colder. This is reasonable for all three molecules, as CH<sub>3</sub>OH peaks in MM1b while CH<sub>3</sub>CN and SO<sub>2</sub> peak in MM1a

**Table 4.** Calculated physical parameters for MM1b from GOBASIC fits. The four parameters are column density in  $\text{cm}^{-2}$  ( $N_{\text{T}}$ ), temperature in K, spectral line full width half maximum in  $\text{km s}^{-1}$  (FWHM), and  $v_{\text{lsr}}$  in  $\text{km s}^{-1}$  ( $v_{\text{lsr}}$ ).

MM1b Derived Parameters				
Molecule	$N_{\text{T}}$ ( $\text{cm}^{-2}$ )	Temperature (K)	FWHM ( $\text{km s}^{-1}$ )	$v_{\text{lsr}}$ ( $\text{km s}^{-1}$ )
CH <sub>3</sub> CN	3.26(0.22)e+16	56.7(0.9)	4.32(0.07)	8.52(0.04)
CH <sub>3</sub> OCH <sub>3</sub>	3.82(0.18)e+17	110.3(5.3)	5.95(0.22)	8.60(0.14)
CH <sub>3</sub> OH	1.17(0.02)e+18	204.7(2.7)	6.80(0.08)	8.25(0.04)
HCOOCH <sub>3</sub>	7.28(0.52)e+16	89.4(5.4)	5.79(0.27)	8.59(0.12)
HNCO	1.51(0.22)e+16	107.1(16.0)	6.55(0.53)	8.92(0.23)
SO <sub>2</sub>	9.11(0.22)e+16	82.8(5.6)	6.93(0.16)	9.56(0.08)

**Table 5.** Calculated physical parameters for MM3 from GOBASIC fits. The four parameters are column density in  $\text{cm}^{-2}$  ( $N_{\text{T}}$ ), temperature in K, spectral line full width half maximum in  $\text{km s}^{-1}$  (FWHM), and  $v_{\text{lsr}}$  in  $\text{km s}^{-1}$  ( $v_{\text{lsr}}$ ).

MM3 Derived Parameters				
Molecule	$N_{\text{T}}$ ( $\text{cm}^{-2}$ )	Temperature (K)	FWHM ( $\text{km s}^{-1}$ )	$v_{\text{lsr}}$ ( $\text{km s}^{-1}$ )
CH <sub>3</sub> CN	8.98(5.09)e+13	112.4(53.3)	3.53(0.85)	13.28(0.54)
HNCO	1.03(0.73)e+15	230.6(125.1)	8.50(2.73)	9.14(1.49)
SO <sub>2</sub>	3.36(0.65)e+15	140.6(27.6)	8.73(0.91)	9.80(0.38)

(Minh et al. 2010; van der Walt et al. 2021). Further discussion of molecular peaks can be found in Section 5. As in MM1a, both FWHM and velocity values are consistent with those found by van der Walt et al. (2021).

Nine molecules were detected in MM2 with lines above  $3\sigma$ : CH<sub>3</sub>CN, CH<sub>3</sub>OCH<sub>3</sub>, CH<sub>3</sub>OH, CS, C<sup>34</sup>S, HCOOCH<sub>3</sub>, H<sub>2</sub>CS, OCS, and SiO. However, these molecules have fewer than ten transitions visible above  $3\sigma$  in the spectrum at the continuum peak for this core. Due to this, it was difficult to obtain an accurate fit for the physical parameters of any of them. To further analyze these molecules, fits were attempted in which temperatures were fixed to the values derived for MM1a and MM1b in order to obtain an estimation for column density. From this, only CH<sub>3</sub>OCH<sub>3</sub> had a derived value for column density that was greater than the uncertainty. Fixed at 110 K, CH<sub>3</sub>OCH<sub>3</sub> had a derived column density of  $9.4(4.2)\times 10^{15} \text{ cm}^{-2}$ . As the other molecules detected in MM2 had uncertainty values greater than the derived parameter values, even when fixing the temperature, they are not listed in a table here.

Seven molecules were detected in MM3 with lines above  $3\sigma$ : CH<sub>3</sub>CN, H<sub>2</sub>CS, HCOOCH<sub>3</sub>, HNCO, OCS, SO, and SO<sub>2</sub>. Physical parameters were obtained for CH<sub>3</sub>CN, HNCO, and SO<sub>2</sub>. These molecules each have numerous lines in the spectrum, enabling a full analysis. The calculated physical parameters for these molecules are shown in Table 5. As in the MM1a and MM1b regions, it was difficult to derive accurate parameters via fitting for other molecules detected in this region due to each molecule having less than five observable lines over  $3\sigma$  that were not affected by blending.

#### 4. PHYSICAL PARAMETER MAPS



In order to better understand how the chemistry changes across a star-forming region, maps of column density, temperature, and velocity were created for molecules that fit well in at least two regions. To do so, a spectrum for both the upper and lower sidebands was extracted from each pixel surrounding MM1a, MM1b, MM2, and MM3. For each specific pixel, the spectra from both sidebands were baseline-corrected with a first-order polynomial using the `imodpoly` algorithm of the `pybaselines`<sup>3</sup> python library and combined to create the finalized spectra to be analyzed using GOBASIC. GOBASIC was then run iteratively through all spectra to fit all molecules simultaneously. This procedure follows that used in Giese et al. (2024) and Thompson et al. (2023) with a key difference: pixels resulting in high uncertainties were not flagged and set to zero. Instead, any fits that hit the upper and lower bounds of the initial user-inputted parameter guesses were set to zero, while fits with high uncertainty were still included.

Maps were created for the six molecules with good fits in the MM1b region, as these were the only molecules that also fit well across MM2 and MM3. Specifically, maps were only created for a given molecule if that molecule had well-fit parameters described in the tables above. Overall, the MM2 and MM3 regions proved difficult to fit due to having a much lower signal-to-noise ratio than MM1, but there is still clear evidence of molecular emission in each region. These maps also show the first known evidence of complex organics in the MM2 region (Minh et al. 2010; van der Walt et al. 2021). The parameter maps for CH<sub>3</sub>CN are shown in Figure 4, while the maps for all other molecules are shown in Appendix B. Full uncertainty maps of each parameter across every pixel are shown in Appendix C. It is also important to note that in both the MM2 and MM3 regions, most pixels have uncertainties greater than the derived parameter values. The analysis of parameters across these two regions using this mapping method should therefore be seen as an initial estimate rather than a quantitative result. For many molecules, there is a clear difference in calculated values between the MM1a and MM1b regions. Furthermore, the parameter maps do not have a 1:1 correlation with the continuum contours. This is further discussed in Section 5.

Generally, the column density for each molecule peaks at either MM1a or MM1b. CH<sub>3</sub>OCH<sub>3</sub>, CH<sub>3</sub>OH, and HCOOCH<sub>3</sub> peak in MM1b, while SO<sub>2</sub> peaks in MM1a. However for CH<sub>3</sub>CN and HNCO, the column density is relatively uniform across both regions. CH<sub>3</sub>OH has the highest column density out of all the molecules of  $1.0 \times 10^{18}$  cm<sup>-2</sup> in MM1b. In MM2 and MM3, all molecules are found to have column densities of approximately an order of magnitude less than those found for MM1. For CH<sub>3</sub>CN and CH<sub>3</sub>OCH<sub>3</sub>, the column density across MM2 is fairly uniform, whereas in CH<sub>3</sub>OH and HCOOCH<sub>3</sub> it increases southward across the continuum core. As is evident in the maps for CH<sub>3</sub>CN and HNCO, MM3 is seemingly split into two parts, with the west side of the region having a higher column density than the east side. Conversely, the map for SO<sub>2</sub> is much more uniform across both sides.

Overall, temperature proved much more difficult to fit in each region. Maps for MM2 and MM3 were most affected due to a considerable intensity difference between these regions and MM1. CH<sub>3</sub>CN and CH<sub>3</sub>OH have the highest temperature values of around 280 K in MM1a and MM2, respectively. Unlike column density, most molecules have higher temperatures in MM1a than in MM1b. Out of the six molecules tested, CH<sub>3</sub>OH is the only molecule with a higher temperature in MM1b. The temperature map of SO<sub>2</sub> shows two areas of the MM1 region where values drop drastically. This may

<sup>3</sup> <https://github.com/derb12/pybaselines>

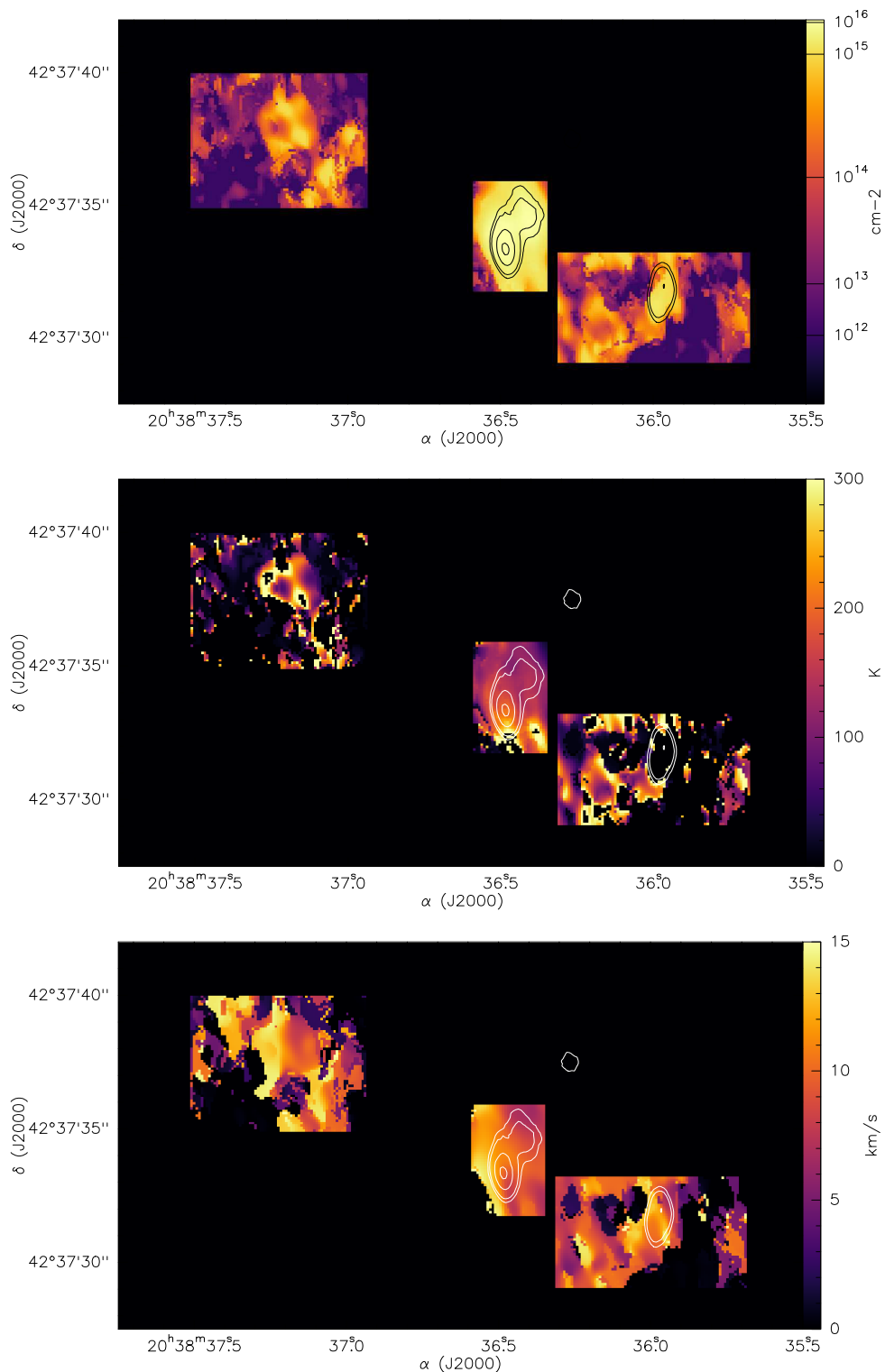


**Figure 4.** Parameter maps for  $\text{CH}_3\text{CN}$  across MM1, MM2, and MM3 (from top to bottom: column density, kinetic temperature, and  $v_{lsr}$ ). Black and white contours correspond to the continuum levels at 2, 3, 7, and 12 times  $\sigma$  ( $\sigma = 3.079 \text{ mJy beam}^{-1}$ ). The colors of the contours are arbitrary and differ between maps purely for aesthetic purposes. In both the MM2 and MM3 regions, most pixels have uncertainties greater than the derived parameter values. The analysis of parameters across these two regions using this mapping method should therefore be seen as an initial estimate rather than a quantitative result.

be due to  $\text{SO}_2$  having some optically thick lines as reported in [van der Walt et al. \(2021\)](#). While there were no optically thick lines found in this analysis, further results would be beneficial in determining the cause of these temperature drops.

The velocity maps show a distinct difference in values when comparing MM1a to MM1b. Across the entirety of MM1, every molecule shows a gradual increase in velocity from around  $5.0 \text{ km s}^{-1}$  to  $15.0 \text{ km s}^{-1}$  west to east. For the case of  $\text{HCOOCH}_3$ , velocity was poorly-derived in MM1a due to a much lower signal-to-noise. In MM2, all molecules show a velocity of around  $10 \text{ km s}^{-1}$  inside the continuum contours. In MM3, the maps for  $\text{CH}_3\text{CN}$  and  $\text{HNCO}$  once again show the split of the region into east and west portions. Both molecules gradually increase in value from around  $10.0 \text{ km s}^{-1}$  to  $15.0 \text{ km s}^{-1}$  west to east.  $\text{SO}_2$ , however, is more uniform in MM3 with a value around  $12.0 \text{ km s}^{-1}$ .

Along with showing how the physical parameters of each molecule change across each region, it is also important to directly compare these parameters between each molecule. Figure 5 compares the calculated column density values of each individual pixel in the MM1 region. Generally, most of the plots show two distinct components based on whether the molecule peaks in MM1a or MM1b. For comparisons in which both molecules peak in either MM1a or MM1b, the relationship is almost linear.  $\text{CH}_3\text{OCH}_3$ ,  $\text{CH}_3\text{OH}$ , and  $\text{HCOOCH}_3$  directly exhibit this feature.  $\text{SO}_2$  correlates the least with the other molecules, most likely due to being the only sulfur molecule analyzed in this manner. Figure 6 directly compares column density and temperature for each molecule. Interestingly, each molecule apart from  $\text{HNCO}$  also individually exhibits two distinct components in line shape, albeit less obvious than seen in Figure 5. For these molecules, one component has higher column density and a lower temperature, and the other component has lower column density and a higher temperature. This gives further evidence that different molecules are more abundant at either MM1a or MM1b.

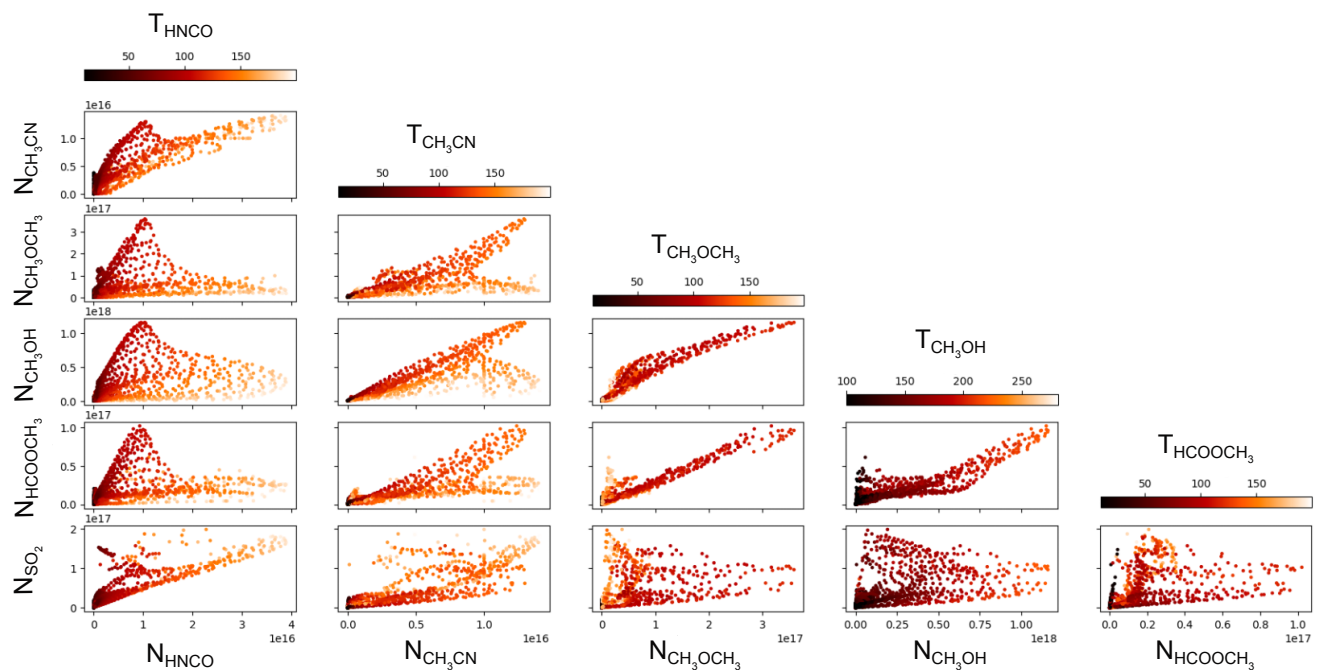


**Figure 5.** Plots comparing column densities in  $\text{cm}^{-2}$  between pairs of molecules across the MM1 region. The color bar denotes temperature in K of the molecule on the x-axis.

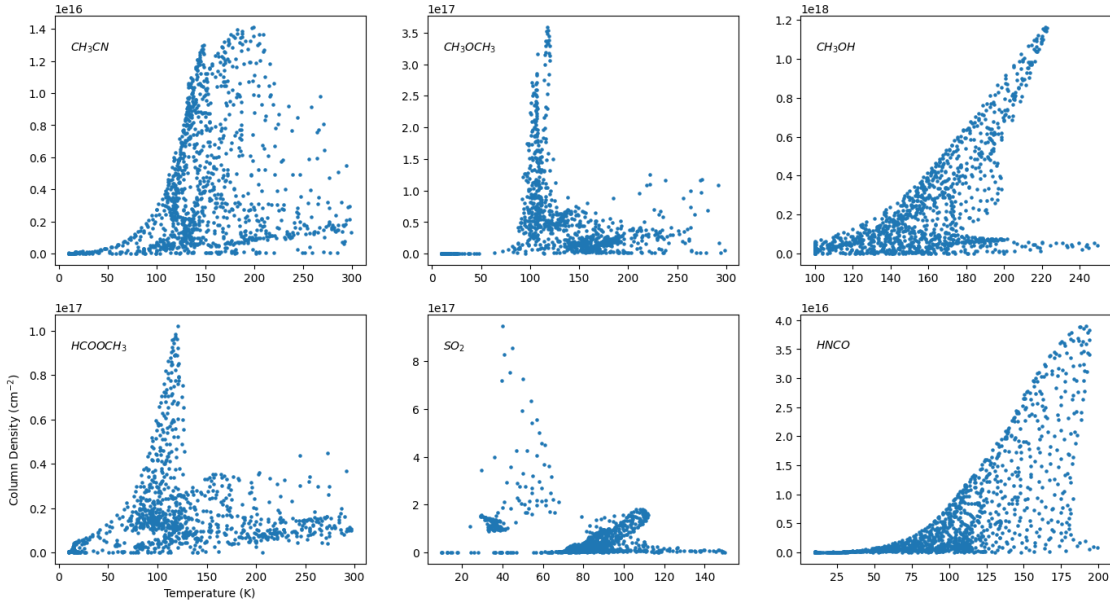


**Figure 6.** Plots comparing column density to temperature for each molecule across the MM1 region.

## 5. DISCUSSION

From the 28 high-resolution windows, molecular emission from MM1, MM2, and MM3 were imaged via moment-0 maps using the Astropy<sup>4</sup> python library. These windows included numerous transitions for multiple molecules, as shown in Table 6, with none of the reported transitions being affected by blending with other spectral lines. While this list describes every transition seen in the high-resolution datacubes, many more transitions and molecules were observed in the two low-resolution datacubes. For each transition seen in the high-resolution windows, emission was integrated over channels above  $3\sigma$ , with the value of  $\sigma$  changing dependent on the imaged cube (described in Appendix A). Stacked moment maps were made for molecules which had multiple transitions throughout all of the high-resolution windows by using a similar process to van der Walt et al. (2021). To do so, each transition was averaged together using a  $1/\sigma^2$  weighting scheme. Every molecule for which this stacking method was used had similar spatial distribution across transitions except for  $\text{CH}_3\text{OH}$ . Although every other methanol transition seen in the 28 high-resolution windows shows compact emission in MM1, the  $9_{0,9}-8_{1,8}$   $A$   $v_t=0$  transition shows extended emission northward of MM1b with high intensity. This transition most likely traces the numerous methanol masers found north of MM1b shown in Figure 27 of Fish et al. (2005). While this transition is not a common indicator of a methanol maser, it has been predicted to be one at medium gas densities (Nesterenok 2021). Due to having a vastly different spatial distribution compared to the other methanol transitions, this transition was not included in the stacking process and was instead imaged separately. Figure 7 shows the moment-0 map of each molecule seen in the high-resolution windows in the MM1 region, along with maps for two unidentified transitions. Due to the MM2 and MM3 regions having significantly lower fluxes

<sup>4</sup> <http://www.astropy.org>

than the MM1 region, separate moment-0 maps were created for molecules detected in these regions. These are shown in Figures 8 and 9. For some molecules in the MM2 region, emission was only seen above  $3\sigma$  in specific transitions. Figure 10 shows the MM1 moment-0 map of the methanol transition that traces the masers.

**Table 6.** Molecular transitions covered in the high-resolution windows.

Molecule	Transition	Rest Frequency (GHz)	$E_u$ (K)	SPW (mJy/beam)	MM2/MM3 <sup>a</sup>	Weighted $\sigma$
CH <sub>3</sub> CN	7 <sub>6</sub> -6 <sub>6</sub>	128.690	281.79	3		4.531
	7 <sub>5</sub> -6 <sub>5</sub>	128.717	203.28	3		
	7 <sub>4</sub> -6 <sub>4</sub>	128.740	139.02	3		
	7 <sub>3</sub> -6 <sub>3</sub>	128.757	89.02	3		
	7 <sub>2</sub> -6 <sub>2</sub>	128.769	53.30	3		
	7 <sub>1</sub> -6 <sub>1</sub>	128.777	31.87	3	MM3	
	8 <sub>6</sub> -7 <sub>6</sub>	147.073	288.84	25		
	8 <sub>5</sub> -7 <sub>5</sub>	147.104	210.34	25		
	8 <sub>4</sub> -7 <sub>4</sub>	147.129	146.08	25		
	8 <sub>3</sub> -7 <sub>3</sub>	147.149	96.08	25		
	8 <sub>2</sub> -7 <sub>2</sub>	147.163	60.36	25		
	8 <sub>1</sub> -7 <sub>1</sub>	147.172	38.93	25		
	8 <sub>0</sub> -7 <sub>0</sub>	147.175	31.79	25	MM2	
CH <sub>3</sub> OCH <sub>3</sub> <sup>b</sup>	11 <sub>3,8</sub> -11 <sub>2,9</sub>	133.268	72.87	9	MM2	4.318
	24 <sub>3,21</sub> -24 <sub>2,22</sub>	133.313	290.14	9		
	12 <sub>2,11</sub> -12 <sub>1,12</sub>	135.267	76.28	14		
	13 <sub>2,12</sub> -13 <sub>1,13</sub>	143.163	88.00	15		
	6 <sub>3,3</sub> -6 <sub>2,4</sub>	144.859	31.77	19		
	26 <sub>4,22</sub> -26 <sub>1,25</sub>	148.119	344.84	26		
	9 <sub>3,7</sub> -9 <sub>2,8</sub>	149.570	53.64	27		
	25 <sub>4,21</sub> -25 <sub>1,24</sub>	150.163	320.68	28		
	21 <sub>2,19</sub> -21 <sub>1,20</sub>	150.594	220.15	28		
CH <sub>3</sub> OH <sup>c</sup>	12 <sub>1,11</sub> -11 <sub>2,10</sub> A $v_t=0$	129.433	197.07	5		4.432
	6 <sub>2,5</sub> -7 <sub>1,6</sub> A $v_t=0$	132.622	86.46	8		
	6 <sub>1,6</sub> -5 <sub>-0,5</sub> E	132.891	54.31	8		
	20 <sub>-4,16</sub> -19 <sub>-5,14</sub> E	133.261	583.10	9		
	5 <sub>2,3</sub> -6 <sub>1,6</sub> E	133.605	60.72	10		
	12 <sub>3,9</sub> -13 <sub>2,11</sub> E	134.231	243.74	11		
	8 <sub>2,7</sub> -7 <sub>3,4</sub> A $v_t=0$	134.897	121.27	12		
	7 <sub>-3,5</sub> -8 <sub>-2,7</sub> E $v_t=0$	143.170	112.71	15		
	3 <sub>2,1</sub> -2 <sub>2,0</sub> E $v_t=2$	144.571	658.82	18		
	3 <sub>0,3</sub> -2 <sub>0,2</sub> A $v_t=2$	144.572	522.08	18		
	3 <sub>-2,2</sub> -2 <sub>-2,1</sub> E $v_t=2$	144.580	600.11	18		

**Table 6.** Molecular transitions covered in the high-resolution windows.

Molecule	Transition	Rest Frequency (GHz)	$E_u$ (K)	SPW (mJy/beam)	MM2/MM3 <sup>a</sup>	Weighted $\sigma$
	3 <sub>1,3</sub> -2 <sub>1,2</sub> E $v_t=2$	144.584	545.90	18		
	3 <sub>1,3</sub> -2 <sub>1,2</sub> A $v_t=1$	144.590	339.14	18		
	3 <sub>2,2</sub> -2 <sub>2,1</sub> A $v_t=1$	144.728	312.57	19		
	3 <sub>2,2</sub> -2 <sub>2,1</sub> E $v_t=1$	144.729	378.50	19		
	3 <sub>2,1</sub> -2 <sub>2,0</sub> A $v_t=1$	144.729	312.57	19		
	3 <sub>-2,1</sub> -2 <sub>-2,0</sub> E $v_t=1$	144.733	413.79	19		
	3 <sub>1,3</sub> -2 <sub>1,2</sub> $v_t=1$	144.735	305.37	19		
	3 <sub>-0,3</sub> -2 <sub>-0,2</sub> E $v_t=1$	144.736	314.46	19		
	3 <sub>1,2</sub> -2 <sub>1,1</sub> E $v_t=1$	144.750	427.27	19		
	3 <sub>0,3</sub> -2 <sub>0,2</sub> A $v_t=1$	144.768	437.54	19		
	3 <sub>1,2</sub> -2 <sub>1,1</sub> A $v_t=1$	144.879	339.16	19		
	3 <sub>-0,3</sub> -2 <sub>-0,2</sub> E $v_t=0$	145.093	27.05	20		
	3 <sub>1,3</sub> -2 <sub>1,2</sub> E $v_t=0$	145.097	19.50	20		
	3 <sub>0,3</sub> -2 <sub>0,2</sub> A $v_t=0$	145.103	13.93	20		
	3 <sub>2,2</sub> -2 <sub>2,1</sub> A $v_t=0$	145.124	51.64	20		
	3 <sub>-2,2</sub> -2 <sub>-2,1</sub> E $v_t=0$	145.126	36.17	20		
	3 <sub>2,1</sub> -2 <sub>2,0</sub> E $v_t=0$	145.126	39.83	20		
	3 <sub>-1,2</sub> -2 <sub>-1,1</sub> E $v_t=0$	145.132	34.97	20		
	3 <sub>2,1</sub> -2 <sub>2,0</sub> A $v_t=0$	145.133	51.64	20		
	3 <sub>1,2</sub> -2 <sub>1,1</sub> A $v_t=0$	146.368	28.59	23		
	9 <sub>0,9</sub> -8 <sub>1,8</sub> A $v_t=0$	146.619	104.41	24		
	15 <sub>-0,15</sub> -15 <sub>1,15</sub> E $v_t=0$	148.112	290.74	26		
	14 <sub>-2,13</sub> -13 <sub>-3,11</sub> E $v_t=0$	149.533	266.13	27		
	14 <sub>-0,14</sub> -14 <sub>1,14</sub> E2 $v_t=0$	150.142	256.14	28	MM2	
CS	3-2	146.969	14.11	25	MM2	
C <sup>34</sup> S	3-2	144.617	11.80	18	MM2	
DCN	2-1	144.828	10.43	19		
H <sub>2</sub> CO	7 <sub>1,6</sub> -7 <sub>1,7</sub>	135.030	112.79	13		4.185
	2 <sub>0,2</sub> -1 <sub>0,1</sub>	145.603	10.48	21		
	2 <sub>1,1</sub> -1 <sub>1,0</sub>	150.498	22.62	28		
H <sub>2</sub> CS	4 <sub>1,4</sub> -3 <sub>1,3</sub>	135.298	29.40	14	MM2	
HC <sub>3</sub> N	16-15	145.561	59.38	21		
HCOOCH <sub>3</sub>	12 <sub>0,12</sub> -11 <sub>0,11</sub>	132.245	42.43	7		4.021
	11 <sub>1,10</sub> -10 <sub>1,9</sub> E	132.922	40.39	8		
	11 <sub>1,10</sub> -10 <sub>1,9</sub> A	132.929	40.38	8		
	11 <sub>7,4</sub> -10 <sub>7,3</sub>	135.290	71.48	14		
	12 <sub>6,6</sub> -11 <sub>6,5</sub>	148.046	69.96	26	MM2	

**Table 6.** Molecular transitions covered in the high-resolution windows.

Molecule	Transition	Rest Frequency (GHz)	$E_u$ (K)	SPW (mJy/beam)	MM2/MM3 <sup>a</sup>	Weighted $\sigma$
	12 <sub>4,8</sub> -11 <sub>4,7</sub> E	150.601	57.04	28		
	12 <sub>4,8</sub> -11 <sub>4,7</sub> A	150.618	57.02	28		
HDO	4 <sub>2,2</sub> -4 <sub>2,3</sub>	143.727	319.17	17		
OCS	12-11	145.947	45.53	22	MM2	
SiO	3-2	130.269	12.50	6		
SO	3 <sub>3</sub> -2 <sub>2</sub>	129.139	25.51	4	MM3	
<sup>33</sup> SO	3 <sub>3</sub> -2 <sub>2</sub>	127.859	25.41	1		
SO <sub>2</sub>	12 <sub>2,10</sub> -12 <sub>1,11</sub>	128.605	82.58	3	MM3	4.438
	12 <sub>1,11</sub> -11 <sub>2,10</sub>	129.106	76.41	4	MM3	
	10 <sub>2,8</sub> -10 <sub>1,9</sub>	129.515	60.93	5	MM3	
	14 <sub>2,12</sub> -14 <sub>1,13</sub>	132.745	108.12	8	MM3	
	10 <sub>4,6</sub> -11 <sub>3,9</sub>	146.550	89.83	24	MM3	
	4 <sub>2,2</sub> -4 <sub>1,3</sub>	146.606	19.03	24	MM3	
<sup>34</sup> SO <sub>2</sub>	8 <sub>2,6</sub> -8 <sub>1,7</sub>	128.669	42.83	3		
Unknown Line	-	132.258	-	7		
	-	143.738	-	17		

<sup>a</sup> All transitions listed in this table were detected toward the MM1 region. However, not all listed transitions were also detected toward the MM2 and MM3 regions. This column denotes in which region the transition was detected above  $3\sigma$  in addition to MM1.

<sup>b</sup> Peaks for CH<sub>3</sub>OCH<sub>3</sub> are in the triplet form, representing the AE/EA, EE, and AA states, with the center peak of the triplet corresponding to the EE state. Therefore, for simplicity, the transitions reported here are that of the EE state.

<sup>c</sup> The 3<sub>2,1</sub>-2<sub>2,0</sub> E  $v_t=2$  and 3<sub>0,3</sub>-2<sub>0,2</sub> A  $v_t=2$  transitions are within astronomical line widths of each other. Similarly, the 3<sub>2,2</sub>-2<sub>2,1</sub> A  $v_t=1$ , 3<sub>2,2</sub>-2<sub>2,1</sub> E  $v_t=1$ , and 3<sub>2,1</sub>-2<sub>2,0</sub> A  $v_t=1$  transitions are within astronomical line widths of each other. Due to severe blending, it is unclear which transition is represented in the spectrum.

As mentioned above, SiO has been known to trace molecular outflows in star-forming regions. Specifically, [Shepherd et al. \(2004\)](#) found that the molecular emission from the  $J = 2-1$  transition extends  $\sim 20''$  southward from the MM1 region. Figure 11, the moment-0 maps for SiO in MM1 and MM2, show similar features to this result. Interestingly, [Minh et al. \(2010\)](#) and [Carrasco-González et al. \(2010\)](#) saw much more compact emission from the  $J = 5-4$ ,  $J = 8-7$ , and  $J = 1-0$  transitions. While both previous results and those presented here show emission peaking around MM1a, there is no direct correlation between SiO emission and previously reported outflows in W75N ([Shepherd et al. 2003, 2004](#)). [Carrasco-González et al. \(2010\)](#) instead proposes that the SiO emission traces a new outflow associated with VLA3.

Previous studies have shown that molecules can generally be grouped into two categories depending on whether their emission peaks in MM1a or MM1b, with the complex organics peaking in MM1b and sulfur-bearing molecules peaking in MM1a ([Minh et al. 2010](#); [van der Walt et al. 2021](#)). The

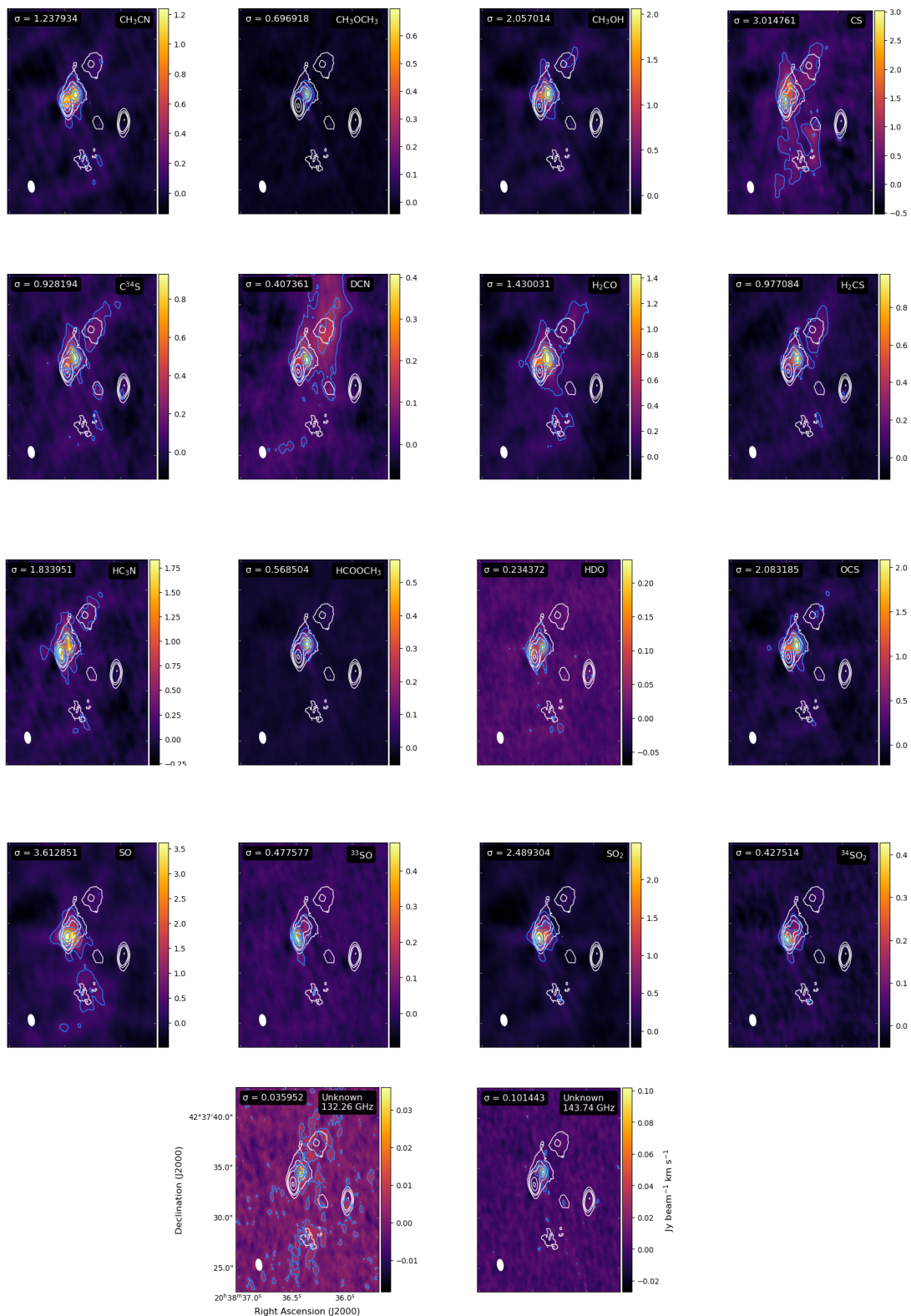


**Figure 7.** Integrated intensity maps of the MM1 region for all molecules seen in the high-resolution windows. For molecules with multiple transitions, the map was created by stacking all transitions together. Blue contour levels correspond to 0.1, 0.3, 0.5, 0.7, and 0.9 times  $\sigma$  (reported in the top left corner). For all molecules, the  $\sigma$  value signifies the maximum flux value reported. White contours correspond to the continuum levels at 1, 2, 3, 7, and 12 times  $\sigma_{cont}$  ( $\sigma_{cont} = 3.079 \text{ mJy beam}^{-1}$ ). Beam size is shown in the bottom left corner.



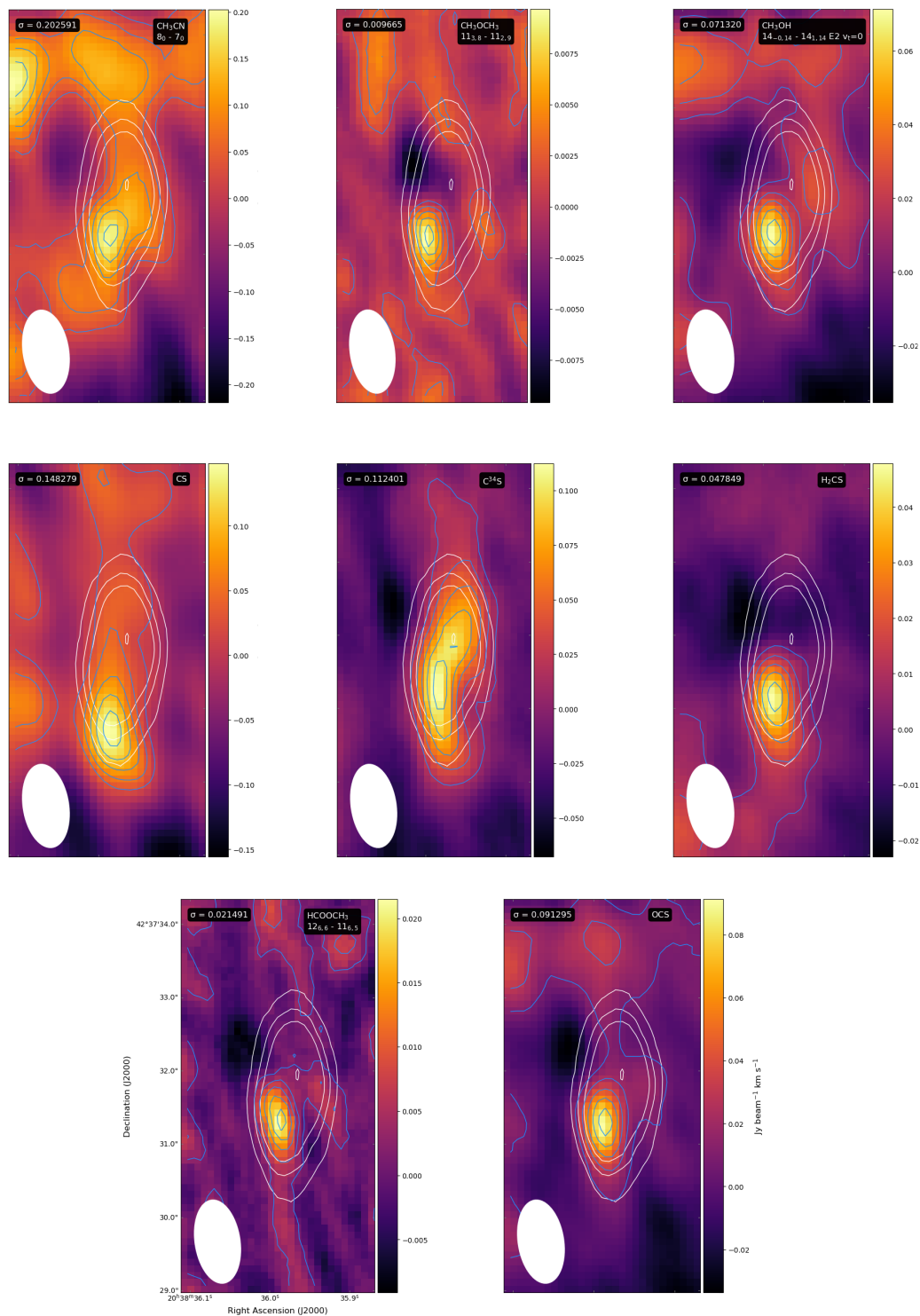


**Figure 8.** Integrated intensity maps of the MM2 region for molecules seen in the high-resolution windows. Blue contour levels correspond to 0.1, 0.3, 0.5, 0.7, and 0.9 times  $\sigma$  (reported in the top left corner). For all molecules, the  $\sigma$  value signifies the maximum flux value reported. White contours correspond to the continuum levels at 1, 2, 3, and 7 times  $\sigma_{\text{cont}}$  ( $\sigma_{\text{cont}} = 3.079 \text{ mJy beam}^{-1}$ ). Beam size is shown in the bottom left corner.

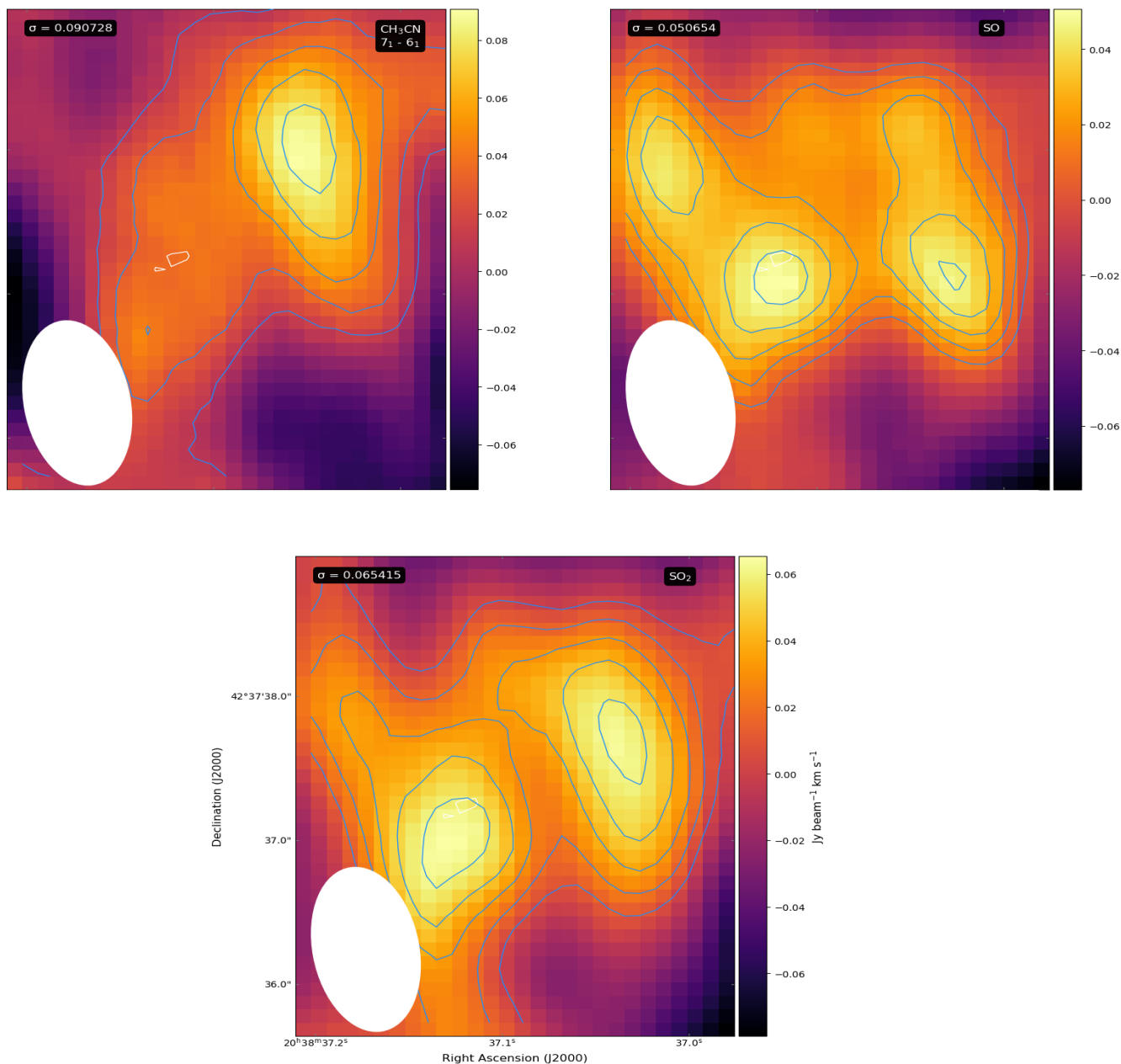


**Figure 9.** Integrated intensity maps of the MM3 region for molecules seen in the high-resolution windows. For molecules with multiple transitions, the map was created by stacking all transitions together. Blue contour levels correspond to 0.1, 0.3, 0.5, 0.7, and 0.9 times  $\sigma$  (reported in the top left corner). For all molecules, the  $\sigma$  value signifies the maximum flux value reported. White contours correspond to the continuum level at 1 times  $\sigma_{\text{cont}}$  ( $\sigma_{\text{cont}} = 3.079 \text{ mJy beam}^{-1}$ ). The map of  $\text{SO}_2$  was creating using the stacking method. Beam size is shown in the bottom left corner.

moment-0 maps presented here support this argument. CS, SiO, SO,  $^{33}\text{SO}$ ,  $\text{SO}_2$ , and  $^{34}\text{SO}_2$  peak in MM1a. DCN,  $\text{CH}_3\text{OCH}_3$ ,  $\text{CH}_3\text{OH}$ ,  $\text{C}^{34}\text{S}$ ,  $\text{H}_2\text{CO}$ ,  $\text{HCOOCH}_3$ ,  $\text{H}_2\text{CS}$ , OCS, and the two unknown lines peak in MM1b. A third category can be used to describe  $\text{CH}_3\text{CN}$ , HDO, and  $\text{HC}_3\text{N } v_7$ , as all

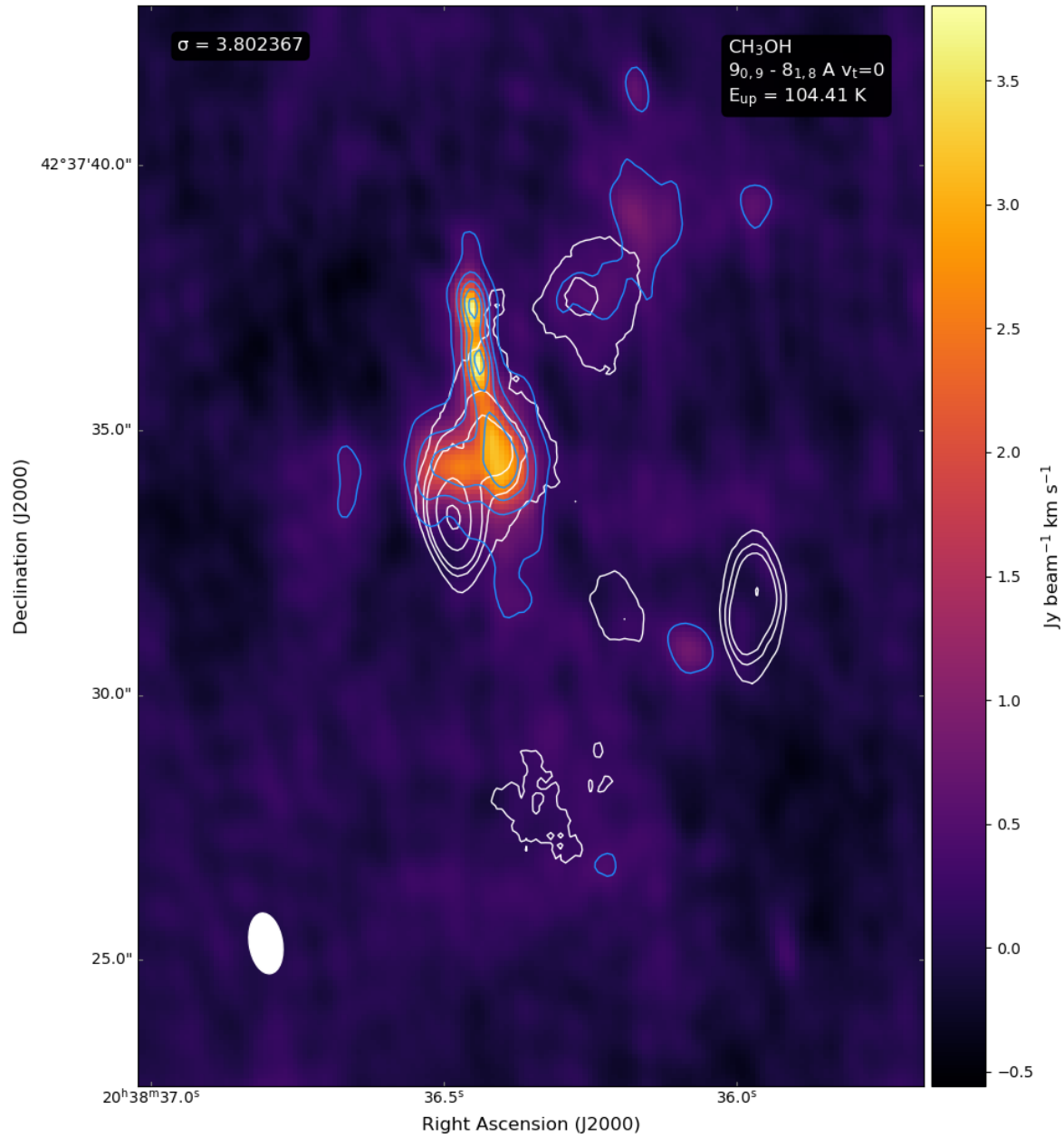


**Figure 10.** Integrated intensity map for the  $\text{CH}_3\text{OH}$  maser seen at 146.619 GHz. Blue contour levels correspond to 0.1, 0.3, 0.5, 0.7, and 0.9 times  $\sigma$  (reported in the top left corner). The  $\sigma$  value signifies the maximum flux value reported. White contours correspond to the continuum levels at 1, 2, 3, 7, and 12 times  $\sigma_{\text{cont}}$  ( $\sigma_{\text{cont}} = 3.079 \text{ mJy beam}^{-1}$ ). Beam size is shown in the bottom left corner.

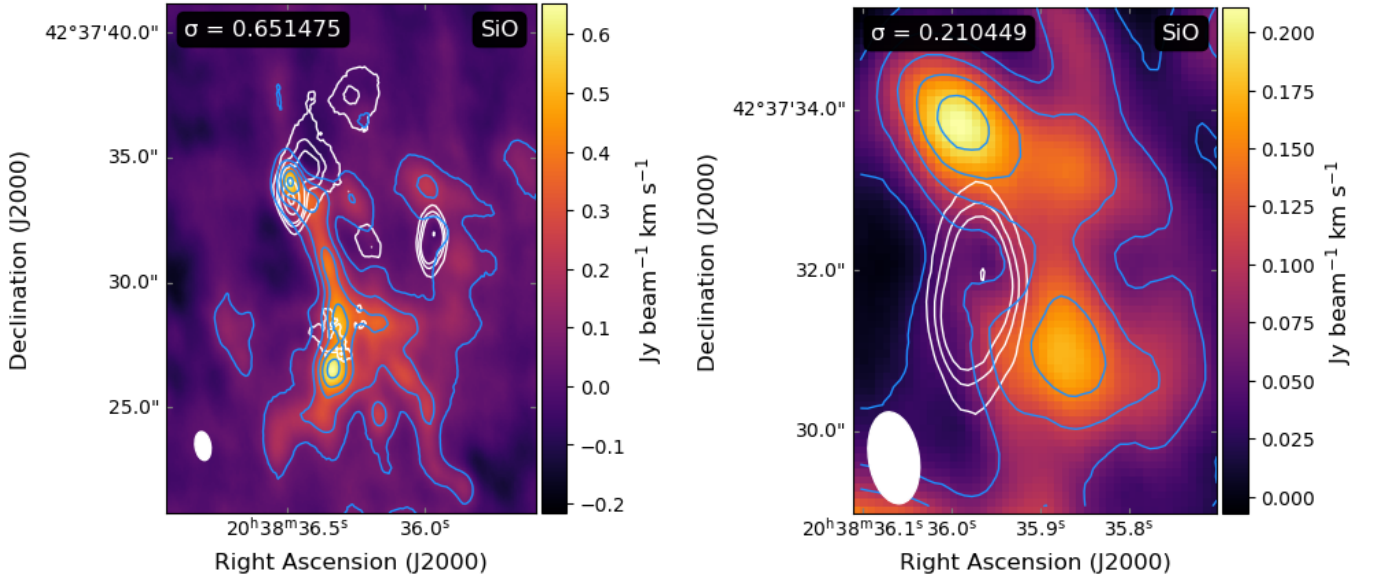


**Figure 11.** Integrated intensity maps for SiO in MM1 (left) and MM2 (right). Blue contour levels correspond to 0.1, 0.3, 0.5, 0.7, and 0.9 times  $\sigma$  (reported in the top left corner). The  $\sigma$  value signifies the maximum flux value reported. White contours correspond to the continuum levels at 1, 2, 3, 7, and 12 times  $\sigma_{cont}$  ( $\sigma_{cont} = 3.079 \text{ mJy beam}^{-1}$ ). Beam size is shown in the bottom left corner.

three show strong emission in both MM1a and MM1b. These results concur with [Minh et al. \(2010\)](#) in that there is a hot core located at MM1b, as complex organic molecules are often tracers of similar sources (e.g. [Blake & van Dishoeck \(1998\)](#)).

For the first time, molecular emission was directly imaged in the MM2 and MM3 region. Every molecule seen in MM2, apart from  $\text{C}^{34}\text{S}$ , shows compact emission on the southern portion of the continuum core.  $\text{C}^{34}\text{S}$ , while peaking in a similar location to the other molecules, has emission extending northward. In MM3, both SO and  $\text{SO}_2$  show two distinct emission peaks. This could be due to the presence of two young stellar objects, as was theorized by [Shepherd \(2001\)](#). The presence of OCS in the spectrum also supports this, as both OCS and SO tend to trace high temperature chemistry in early hot cores ([Wakelam et al. 2004](#); [Tychoniec et al. 2021](#)). All molecules in both MM2 and MM3 only show emission at a level roughly an order of magnitude lower than that in MM1.

Figures 12, 13, and 14 show the calculated Pearson cross-correlation coefficient between each pair of moment-0 maps and the continuum for each region. This coefficient measures the linear correlation of molecular emission between molecules on a spatial scale, with the emission being more similar as the coefficient goes to a value of one. This method has been used in multiple other works to study the chemistry of star-forming regions on a spatial scale ([Guzmán et al. 2018](#); [Law et al. 2021](#); [Thompson et al. 2023](#)). However, it is also important to note that a high correlation coefficient does not intrinsically imply a chemical link between molecules. To calculate this value for the MM1 region, a mask was defined that encompassed a right ascension of  $20^{\text{h}}38^{\text{m}}36.3^{\text{s}} - 36.7^{\text{s}}$  and a declination of  $42^{\circ}37'38''.2 - 31''.9$  in order to account for both MM1a and MM1b. For the MM2 and MM3 regions, this mask was defined with the same boundaries as their respective moment-0 maps. The cross-correlation coefficient was calculated using the pixels within these masks. For the MM1 region, in addition to the maps shown in Figure 7 and the continuum, molecules were also correlated with the

moment-0 map of the CH<sub>3</sub>OH maser-tracing transition. SiO was not included in this analysis for any region due to its high-intensity extended features not seen in any other molecule. Due to the low total flux in both the MM2 and MM3 regions, creating a correlation matrix for molecules proved to be difficult. At such levels, emission from outside the continuum contours has a much larger affect on the correlation. While further observations on the MM2 and MM3 regions are needed to understand the spatial complexity of present molecules, an initial analysis was performed here.

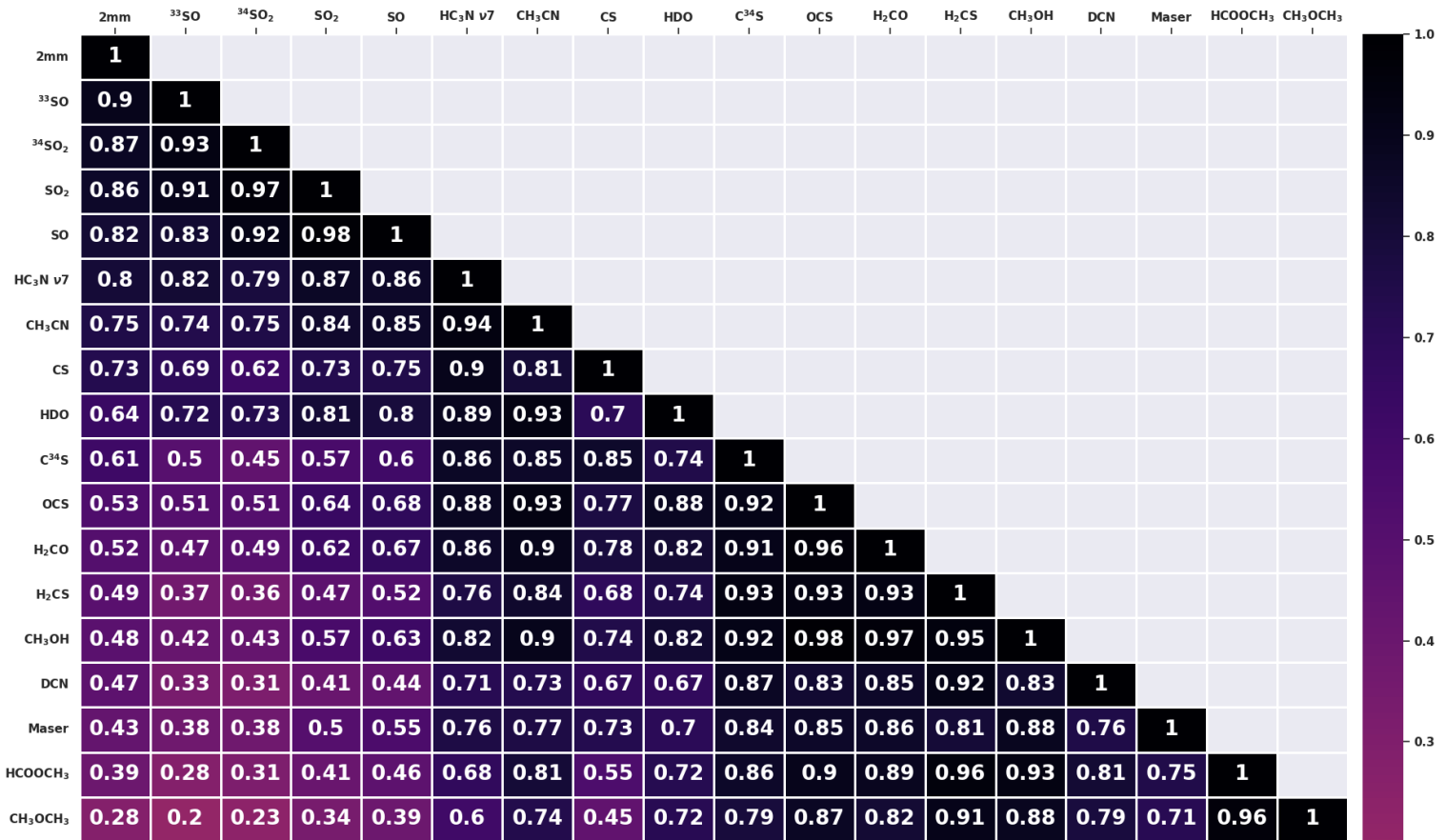


**Figure 12.** Correlation matrix of the MM1 region using the integrated intensity maps shown in Figure 7, the 130 GHz continuum labeled as "2mm", and the integrated intensity map of the CH<sub>3</sub>OH maser-tracing transition at 146.619 GHz labeled as "Maser".

As expected, the pairs of molecules that correlate well across MM1 are those that peak in either MM1a or MM1b. Most of the sulfur-bearing molecules, which peak in MM1a, have strong correlations with one another and the continuum. All of the organic molecules, which peak in MM1b, have strong correlations with one another and weak correlations with the continuum. This spatial differentiation between the organics and sulfur-bearing molecules implies that MM1a and MM1b are

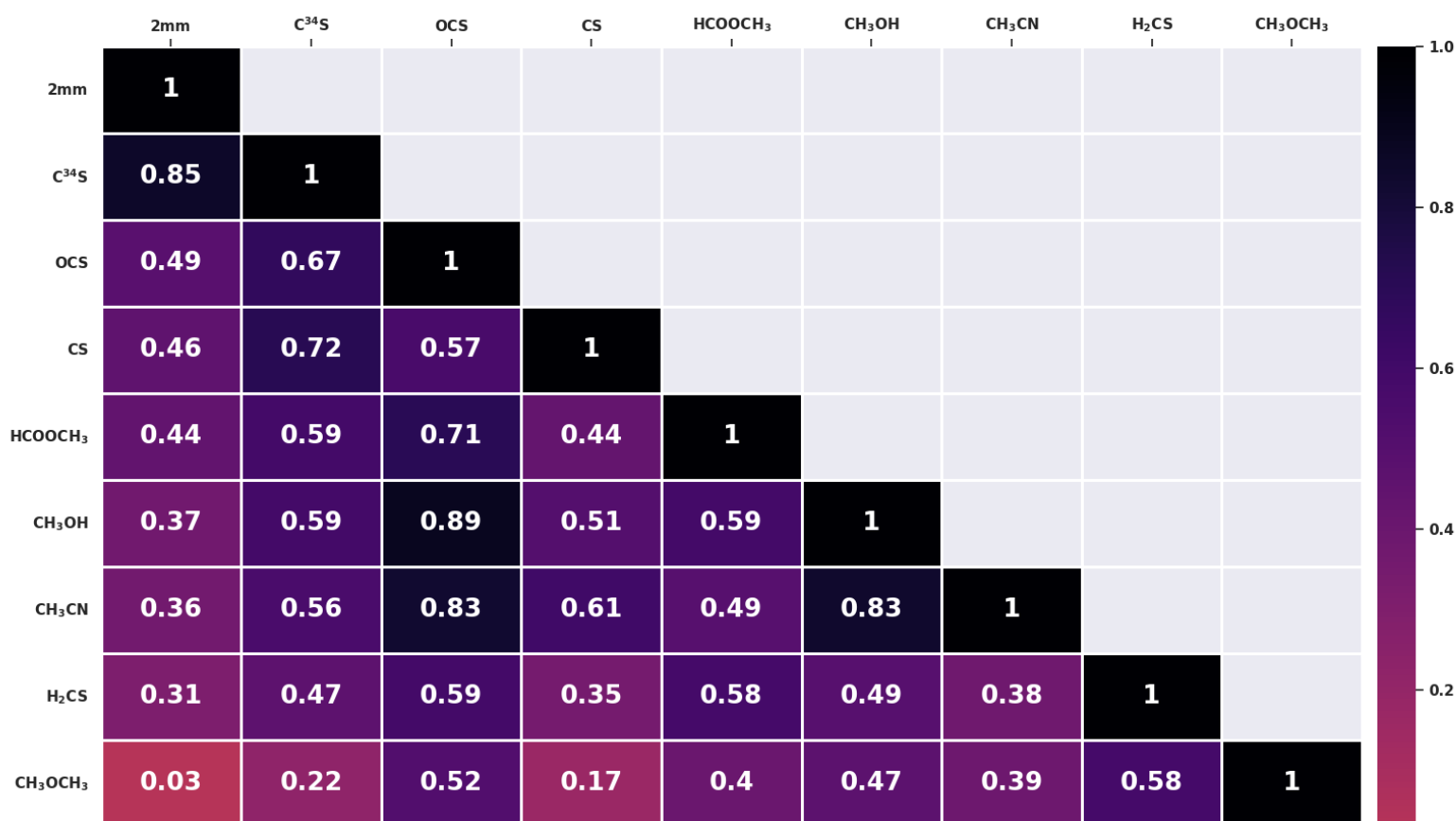


**Figure 13.** Correlation matrix of the MM2 region using the integrated intensity maps shown in Figure 8 and the 130 GHz continuum labeled as "2mm".

at different stages of evolution, with MM1b being the younger of the two (van der Walt et al. 2021). Organic molecules in hot cores can be formed from ultraviolet radiation photoprocessing and thermal processing of ices (Munoz Caro et al. 2002; Herbst & van Dishoeck 2009; Öberg et al. 2011; Altwegg et al. 2019). Conversely, the abundance of sulfur-bearing molecules in MM1a is potentially indicative of hot gas-phase chemistry due to shocks. Shocks have been seen to affect sulfuric chemistry in numerous other sources via multiple reactions, including the enhancement of SO, the increase of S<sup>+</sup>, and the release of sulfur from H<sub>2</sub>S (Charnley 1997; Minh et al. 2010; Guzmán et al. 2018; Thompson et al. 2023). These shocks are also evident due to the extended SiO emission, as SiO is known to trace shocked regions of gas (Hartquist et al. 1980; Minh et al. 2010).

Most molecules in MM2 have relatively low correlation values when compared to those seen in MM1. The three molecules that give the highest correlation are CH<sub>3</sub>CN, CH<sub>3</sub>OH, and OCS, which also are correlated highly in MM1. CH<sub>3</sub>OCH<sub>3</sub> is least correlated with the other molecules, likely due to having

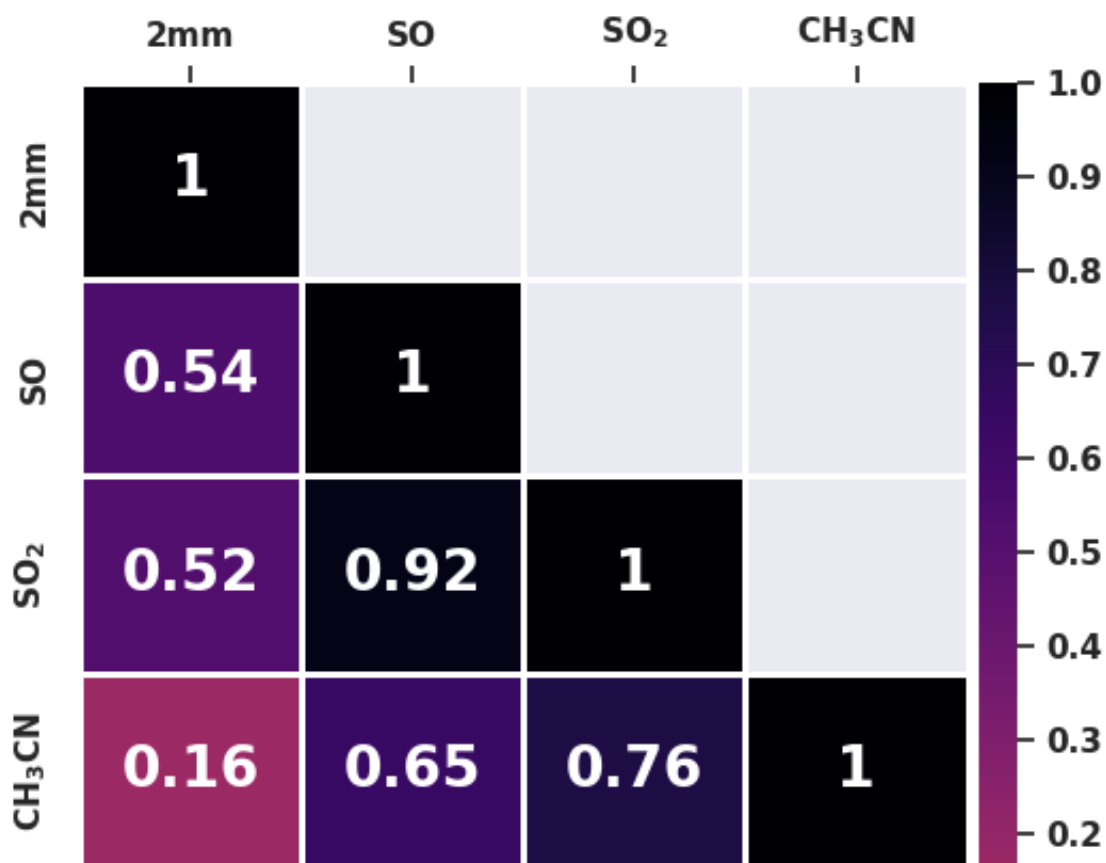


**Figure 14.** Correlation matrix of the MM3 region using the integrated intensity maps shown in Figure 9 and the 130 GHz continuum labeled as "2mm".

emission at the lowest flux values. In MM3, SO and SO<sub>2</sub> have a much higher correlation value with each other as opposed to with CH<sub>3</sub>CN. This is expected as both are sulfur-bearing molecules.

The results for W75N presented here are part of a NOEMA survey to follow-up on the single-dish observations of [Widicus Weaver et al. \(2017\)](#). Previously, [Thompson et al. \(2023\)](#) and [Giese et al. \(2024\)](#) analyzed the molecular composition of the neighboring cores W3(H<sub>2</sub>O) and W3(OH) in the W3 high-mass star-forming region. In the analysis of W3, six molecules accounted for the majority of lines seen across both cores: CH<sub>3</sub>CH<sub>2</sub>CN, CH<sub>3</sub>CN, CH<sub>3</sub>OCH<sub>3</sub>, CH<sub>3</sub>OH, HCOOCH<sub>3</sub>, and SO<sub>2</sub>. Of these molecules, all but CH<sub>3</sub>CH<sub>2</sub>CN are also abundant in the MM1 core of W75N, allowing for direct comparison of column densities and temperatures between the molecules in these two sources. CH<sub>3</sub>CN, CH<sub>3</sub>OH, and SO<sub>2</sub> all have higher column densities in MM1 than in W3, while the column densities of CH<sub>3</sub>OCH<sub>3</sub> and HCOOCH<sub>3</sub> were comparable. Further abundance comparisons between sources will be performed in a future analysis once more sources are studied. Generally, all molecules showed similar temperatures between the two sources. However, HCOOCH<sub>3</sub> was much hotter in W3 with temperatures peaking ~160 K, in contrast with the derived temperature of ~90 K in the continuum peak of MM1b.

While the comparisons between sources are useful, an important difference must be acknowledged when making direct comparisons between the two W3 cores and between the MM1a and MM1b regions. In [Thompson et al. \(2023\)](#), the analysis showed that although W3(H<sub>2</sub>O) and W3(OH) had distinct chemical inventories and molecular properties, the two cores generally showed similar results. However, the two sub-regions MM1a and MM1b instead have vastly different chemical inventory and derived parameters. This demonstrates that each star forming region may have unique chemical mechanisms at play, the physical origins of which have yet to be determined. Our larger survey project that combines single-dish and interferometric observations of all 30 sources examined by ([Widicus Weaver et al. 2017](#)) will hopefully reveal what might be driving these differences. Further results from other sources in our ongoing NOEMA observations will allow for a more comprehensive comparative analysis.

## 6. SUMMARY

We have observed the W75N star-forming region using the IRAM/NOEMA interferometer and analyzed the chemical composition and distribution in the MM1, MM2, and MM3 continuum cores. The broadband spectra extracted toward each core were analyzed with GOBASIC to identify over twenty molecules across the entire region, with the first chemical analysis of this kind being done on MM2 and MM3. COMs were detected in these two cores for the first time. Column density, rotational temperature, and velocity maps were created to spatially characterize six different molecules across the entire region. From these maps, we find a high correlation in the column densities of CH<sub>3</sub>OCH<sub>3</sub>, CH<sub>3</sub>OH, and HCOOCH<sub>3</sub>. The results for MM1a and MM1b generally agree with previous works on W75N ([Minh et al. 2010](#); [Widicus Weaver et al. 2017](#); [van der Walt et al. 2021](#)). Like these previous works, we also find a distinct difference in chemical composition between MM1a and MM1b, with most sulfur-bearing molecules tracing MM1a and most COMs tracing MM1b. Additionally, we created moment-0 maps for seventeen molecules, two unidentified lines, and a maser-tracing methanol transition found in the 28 high-resolution windows. This includes the first imaging of molecular emission in MM2 and MM3. By comparing all of the moment-0 maps in the MM1 region using a Pearson correlation coefficient analysis, the results further support the differentiation between MM1a and MM1b. We find that MM1b likely hosts a hot core with rich COM chemistry, whereas MM1a is affected by shocks, causing SiO emission to trace southward from the region. We also performed an initial correlation analysis on the MM2 and MM3 regions, although further observations are necessary in order to better understand the spatial complexity of these cores. Finally, when comparing results to those of the W3 star-forming region given by [Thompson et al. \(2023\)](#) and [Giese et al. \(2024\)](#), we find similarity in which molecules were detected, although with differing physical parameters and distribution trends. These results indicate that there is a physical mechanism driving chemical differentiation in star-forming cores, the origin of which has yet to be determined.

## 7. ACKNOWLEDGEMENTS

S.L.W.W., M.M.G., and W.E.T. thank the University of Wisconsin–Madison for S.L.W.W.’s startup support and access to NOEMA time that enabled this research. We thank Orsolya Fehér from IRAM for support in setting up the observations and initial data reduction. Part of this research was carried out at the Jet Propulsion Laboratory, California Institute of Technology, under a contract with the National Aeronautics and Space Administration (80NM0018D0004).

*Software:* Astropy ([Astropy Collaboration et al. 2013, 2018, 2022](#)), pybaselines ([Erb 2024](#))



**Table 7.** Summary of High-Resolution Spectral Windows

Spectral Window	Frequency Range (GHz)	RMS (mJy beam <sup>-1</sup> )
1	127.823 - 127.888	4.62
2	127.950 - 128.080	4.96
3	128.589 - 128.849	4.52
4	129.103 - 129.168	4.40
5	129.354 - 129.746	4.22
6	130.190 - 130.319	3.08
7	132.239 - 132.303	3.34
8	132.557 - 132.944	3.90
9	133.133 - 133.328	3.79
10	133.382 - 133.647	3.84
11	134.157 - 134.287	3.79
12	134.861 - 134.926	3.90
13	134.989 - 135.055	3.92
14	135.245 - 135.311	4.06
15	143.116 - 143.181	3.87
16	143.435 - 143.566	4.10
17	143.692 - 143.756	3.91
18	144.522 - 144.653	4.37
19	144.714 - 144.910	4.75
20	145.036 - 145.163	4.55
21	145.547 - 145.612	4.45
22	145.931 - 145.996	4.43
23	146.315 - 146.379	4.39
24	146.507 - 146.635	4.42
25	146.954 - 147.213	4.54
26	148.042 - 148.172	4.66
27	149.514 - 149.579	5.32
28	150.091 - 150.666	5.64

## APPENDIX

## A. SPECTRAL WINDOW SUMMARY

A summary of the observational setup is shown in Table 7. The frequency range of all 28 spectral windows is reported along with the RMS value of each cube. This RMS value was used when creating the moment maps as described above.

## B. PARAMETER MAP FIGURES

This section provides the parameter maps for the five molecules that fit in both MM1 and either MM2 or MM3. The complete figure set (5 images) is available in the online journal.

**Fig. Set 15. Parameter Maps**

## C. UNCERTAINTY MAPS

This section provides uncertainty values for the physical parameters derived using GOBASIC. For each individual pixel and parameter in Figure 4 and Figures 15, the derived values were divided by the corresponding uncertainty. Figures 16 plot these fractions spatially on a logarithmic scale with the more negative values in the plot corresponding to higher fractional uncertainty. The complete figure set (6 images) is available in the online journal.

**Fig. Set 16. Uncertainty Maps**

## REFERENCES

- Altwegg, K., Balsiger, H., & Fuselier, S. A. 2019, *Annual Review of A&A*, 57, 113
- Astropy Collaboration, Robitaille, T. P., Tollerud, E. J., et al. 2013, *A&A*, 558, A33
- Astropy Collaboration, Price-Whelan, A. M., Sipőcz, B. M., et al. 2018, *AJ*, 156, 123
- Astropy Collaboration, Price-Whelan, A. M., Lim, P. L., et al. 2022, *ApJ*, 935, 167
- Blake, G. A., & van Dishoeck, E. F. 1998, *Annual Review of A&A*, 36, 317
- Carrasco-González, C., Rodríguez, L. F., Torrelles, J. M., Anglada, G., & González-Martín, O. 2010, *The Astronomical Journal*, 139, 2433, doi: [10.1088/0004-6256/139/6/2433](https://doi.org/10.1088/0004-6256/139/6/2433)
- Charnley, S. B. 1997, *ApJ*, 481, 396
- Cortes, P. C., Vlahakis, C., Hales, A., et al. 2024, *ALMA Technical Handbook*, Doc. 11.3 ver. 1.4, doi: [10.5281/zenodo.4511521](https://doi.org/10.5281/zenodo.4511521)
- Erb, D. 2024, *pybaselines: A Python library of algorithms for the baseline correction of experimental data*, 1.1.0, doi: [10.5281/zenodo.5608581](https://doi.org/10.5281/zenodo.5608581)
- Fish, V. L., Reid, M. J., Argon, A. L., & Zheng, X. 2005, *ASTROPHYS J SUPPL S*, 160, 220, doi: [10.1086/431669](https://doi.org/10.1086/431669)
- Giese, M. M., Thompson, W. E., Lis, D. C., & Weaver, S. L. W. 2024, *ApJ*, 960, 6, doi: [10.3847/1538-4357/ad08b6](https://doi.org/10.3847/1538-4357/ad08b6)
- Guzmán, A. E., Guzmán, V. V., Garay, G., Bronfman, L., & Hechenleitner, F. 2018, *ApJS*, 236, 45
- Hartquist, T. W., Dalgarno, A., & Oppenheimer, M. 1980, *ApJ*, 236, 182, doi: [10.1086/157731](https://doi.org/10.1086/157731)
- Haschick, A. D., Reid, M. J., Burke, B. F., Moran, J. M., & Miller, G. 1981, *ApJ*, 244, 76, doi: [10.1086/158686](https://doi.org/10.1086/158686)
- Herbst, E., & van Dishoeck, E. F. 2009, *Annual Review of A&A*, 47, 427
- Hunter, T. R., Taylor, G. B., Felli, M., & Tofani, G. 1994, *Astronomy and Astrophysics*, 284, 215, <https://ui.adsabs.harvard.edu/abs/1994A&A...284..215H>
- Hutawarakorn, B., Cohen, R., & Brebner, G. 2002, *Monthly Notices of the Royal Astronomical Society*, 330, 349, doi: [10.1046/j.1365-8711.2002.05068.x](https://doi.org/10.1046/j.1365-8711.2002.05068.x)
- Jørgensen, J. K., Hogerheijde, M. R., Blake, G. A., et al. 2004, *A&A*, 415, 1021
- Law, C. J., Zhang, Q., Öberg, K. I., et al. 2021, *ApJ*, 909, 214
- Minh, Y. C., Su, Y.-N., Chen, H.-R., et al. 2010, *ApJ*, 723, 1231
- Minier, V., Conway, J. E., & Booth, R. S. 2001, *A&A*, 369, 278, doi: [10.1051/0004-6361:20010124](https://doi.org/10.1051/0004-6361:20010124)
- Müller, H., Schlöder, F., Stutzki, J., & Winnewisser, G. 2005, *Journal of Molecular Structure*, 742, 215
- Müller, H., Thorwirth, S., Roth, D. A., & Winnewisser, G. 2001, *A&A*, 370, L49
- Munoz Caro, G. M., Meierhenrich, U., Schutte, W., et al. 2002, *Nature*, 416, 403
- Nesterenok, A. V. 2021, *Journal of Physics: Conference Series*, 2103, 012012
- Öberg, K. I., Boogert, A. C., Pontoppidan, K. M., et al. 2011, *Astrophysical Journal*, 740
- Pickett, H., Poynter, R., Cohen, E., et al. 1998, *Journal of Quantitative Spectroscopy and Radiative Transfer*, 60, 883
- Rad, M. L., Zou, L., Sanders, J. L., & Widicus Weaver, S. L. 2016, *A&A*, 585, 1

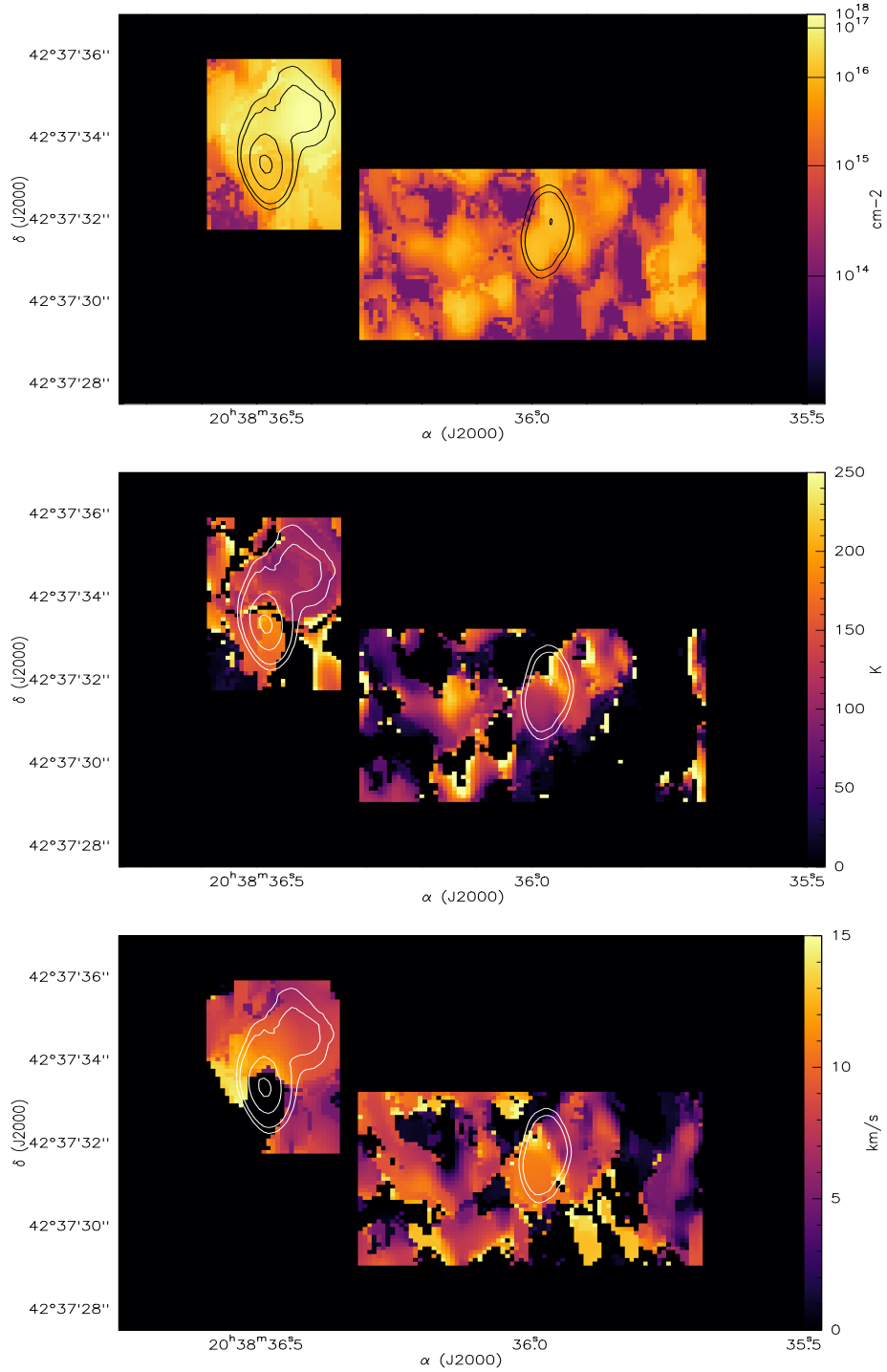


**Figure 15.** Parameter maps for  $\text{CH}_3\text{OCH}_3$  across MM1 and MM2 (from top to bottom: column density, kinetic temperature, and  $v_{lSR}$ ). Black and white contours correspond to the continuum levels at 2, 3, 7, and 12 times  $\sigma$  ( $\sigma = 3.079 \text{ mJy beam}^{-1}$ ). The colors of the contours are arbitrary and differ between maps purely for aesthetic purposes. In the MM2 region, most pixels have uncertainties greater than the derived parameter values. The analysis of parameters across this region using this mapping method should therefore be seen as an initial estimate rather than a quantitative result.

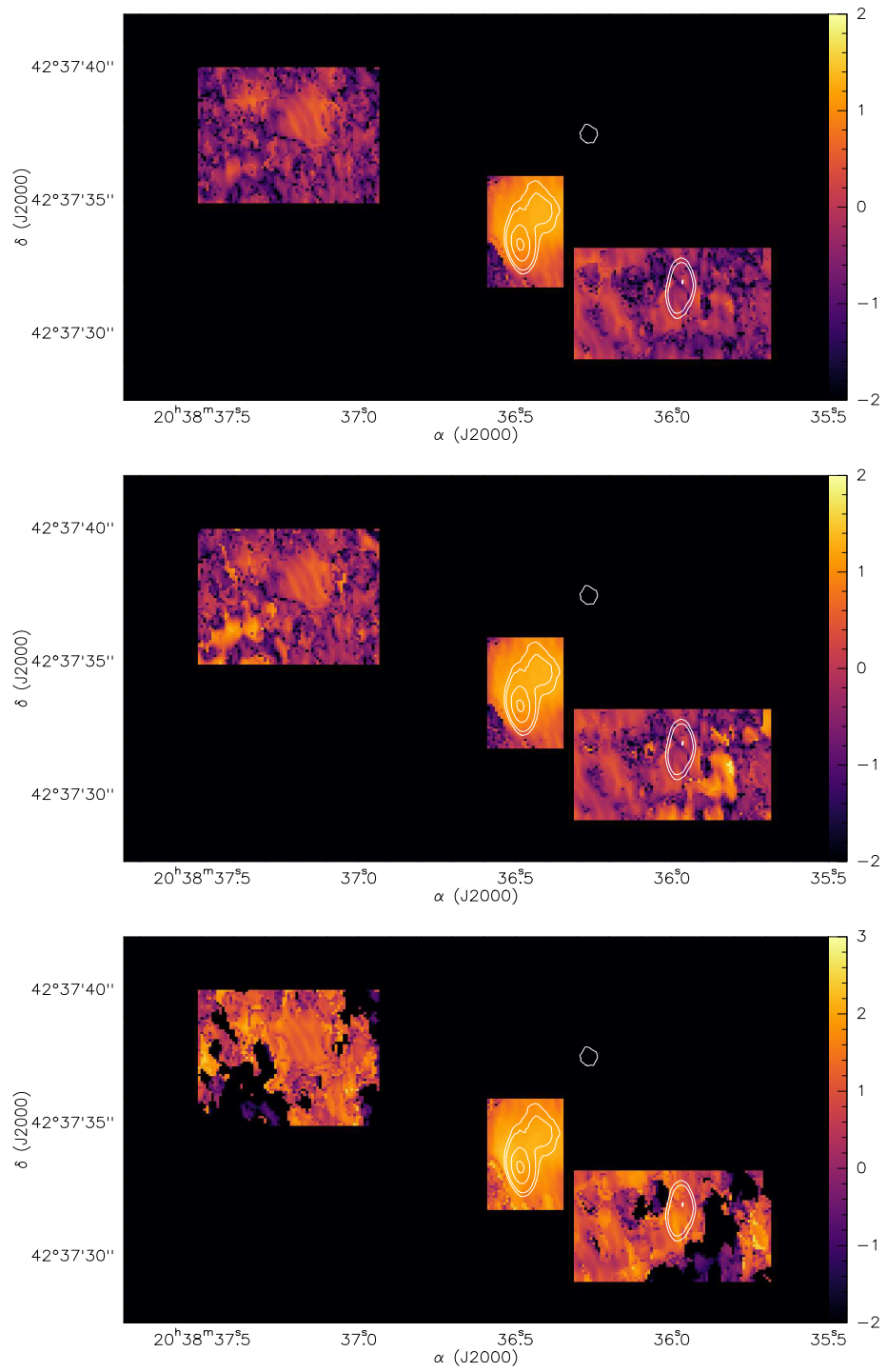


**Figure 16.** Maps describing the uncertainty of parameter values for  $\text{CH}_3\text{CN}$ . See the C for an in-depth description of the map.

- Sánchez-Monge, Á., Schilke, P., Ginsburg, A., Cesaroni, R., & Schmiedeke, A. 2018, *A&A*, 609, A101
- Shepherd, D. S. 2001, *ApJ*, 546, 345
- Shepherd, D. S., Kurtz, S. E., & Testi, L. 2004, *The Astrophysical Journal*, 601, 952, doi: [10.1086/380633](https://doi.org/10.1086/380633)
- Shepherd, D. S., Testi, L., & Stark, D. P. 2003, *ApJ*, 584, 882, doi: [10.1086/345743](https://doi.org/10.1086/345743)
- Surcis, G., Vlemmings, W. H. T., Dodson, R., & Van Langevelde, H. J. 2009, *A&A*, 506, 757, doi: [10.1051/0004-6361/200912790](https://doi.org/10.1051/0004-6361/200912790)
- Thompson, W. E., Giese, M. M., Lis, D. C., & Widicus Weaver, S. L. 2023, *ApJ*, 952, 50
- Tobin, J. J., Hartmann, L., Chiang, H. F., et al. 2011, *Astrophysical Journal*, 740
- Torrelles, J. M., Patel, N. A., Anglada, G., et al. 2003, *ApJ*, 598, L115, doi: [10.1086/380750](https://doi.org/10.1086/380750)
- Tychoniec, L., van Dishoeck, E. F., Van 'T Hoff, M. L., et al. 2021, *A&A*, 655
- van der Walt, S. J., Kristensen, L. E., Jørgensen, J. K., et al. 2021, *A&A*, 655, A86, doi: [10.1051/0004-6361/202039950](https://doi.org/10.1051/0004-6361/202039950)
- van Dishoeck, E. F. 2006, *Proceedings of the National Academy of Sciences of the United States of America*, 103, 12249
- Wakelam, V., Caselli, P., Ceccarelli, C., Herbst, E., & Castets, A. 2004, *A&A*, 422, 159
- Widicus Weaver, S. L., Laas, J. C., Zou, L., et al. 2017, *ApJS*, 232, 3
- Wright, C. J., Smith, R. N., Kroll, J. A., Shipman, S. T., & Widicus Weaver, S. L. 2022, *ACS Earth and Space Chemistry*, 6, 482
- Zeng, L., Zhang, Q., Alves, F. O., et al. 2023, *ApJ*, 954, 99, doi: [10.3847/1538-4357/ace690](https://doi.org/10.3847/1538-4357/ace690)
- Zou, L., & Widicus Weaver, S. L. 2017, *ApJ*, 849, 139